

## Article

# Geochemical Characteristics of Garnet from Zinc–Copper Ore Bodies in the Changpo–Tongkeng Deposit and Its Geological Significance

Lei He <sup>1,2</sup> , Ting Liang <sup>1,2,\*</sup>, Denghong Wang <sup>3,\*</sup>, Zheng Zhao <sup>3</sup>, Bosheng Liu <sup>4</sup>, Jinggao Gao <sup>1,2</sup> and Jubiao Cen <sup>1,2</sup>

<sup>1</sup> School of Earth Science and Resources, Chang'an University, Xi'an 710054, China; 2020027006@chd.edu.cn (L.H.); jggao@chd.edu.cn (J.G.); cenjubiao@foxmail.com (J.C.)

<sup>2</sup> Laboratory of Mineralization and Dynamics, Chang'an University, Xi'an 710054, China

<sup>3</sup> MNR Key Laboratory of Metallogeny and Mineral Assessment, Institute of Mineral Resources, Chinese Academy of Geological Sciences, Beijing 100037, China; kevin8572@hotmail.com

<sup>4</sup> Guangxi 215 Geological Team Co., Ltd., Liuzhou 545002, China; bosheng080910@163.com

\* Correspondence: liangt@chd.edu.cn (T.L.); wangdenghong@vip.sina.com (D.W.)

**Abstract:** The Changpo–Tongkeng tin polymetallic deposit in Dachang, Guangxi, is a world-class, superlarge, polymetallic tin deposit consisting of lower skarn zinc–copper ore bodies and upper tin polymetallic ore bodies. Garnet is the main gangue mineral in the skarn zinc–copper ore bodies and has a granular texture. Based on hand specimens and microscopic observations, the existing garnet can be divided into two generations: an early generation (Grt I) and a late generation (Grt II). The results of electron probe microanalysis (EPMA) and laser ablation-inductively coupled plasma-mass spectrometry (LA-ICP-MS) in situ microanalysis show that the contents of SiO<sub>2</sub> and CaO in the garnets from the two generations present limited variations, while the FeO<sup>T</sup> and Al<sub>2</sub>O<sub>3</sub> contents vary significantly, indicating the grossular–andradite solid solution series (Gro<sub>29–82</sub>And<sub>12–69</sub>). Compared with Grt I (Gro<sub>72</sub>And<sub>25</sub>), Grt II (Gro<sub>39</sub>And<sub>59</sub>) is Fe-enriched and oscillatory zoning is developed. The total rare earth element (REE) contents in the two generations of garnet are relatively low, showing light rare earth element (LREE) depletion and heavy rare earth element (HREE) enrichment patterns. Grt II has higher REE content than Grt I and exhibits significant negative Eu anomalies ( $\delta\text{Eu} = 0.18\text{--}0.44$ ). The contents and variation characteristics of the major and trace elements in the two generations of garnet suggest that there were variable redox conditions and water/rock ratios in the hydrothermal system during the crystallization process of garnet. In the early stage, skarnization was in a relatively closed and low-oxygen fugacity system, with hydrothermal diffusion metasomatism being dominant, forming homogeneous Grt I lacking well-developed zoning. In the late stage of skarnization, the oxygen fugacity of the ore-forming fluids increased, with infiltration metasomatism being dominant, forming Grt II with well-developed oscillatory zoning. The contents of Sn, As, W, In, and Ge in the garnets are relatively high and increase with the proportion of andradite. Sn in zinc–copper ore bodies mainly exists in the form of isomorphic substitution in garnet, which may be the main reason for the lack of tin ore bodies during the skarn stage. This paper compares the trace element contents in garnets from domestic skarn deposits. The results indicate that the Sn content and  $\delta\text{Eu}$  in garnet can be used to evaluate the tin-forming potential of skarn deposits.

**Keywords:** Dachang ore field; zinc–copper ore bodies; garnet; ore-forming fluid evolution



**Citation:** He, L.; Liang, T.; Wang, D.; Zhao, Z.; Liu, B.; Gao, J.; Cen, J. Geochemical Characteristics of Garnet from Zinc–Copper Ore Bodies in the Changpo–Tongkeng Deposit and Its Geological Significance. *Minerals* **2023**, *13*, 937. <https://doi.org/10.3390/min13070937>

Academic Editor: Evgeny Galuskin

Received: 19 June 2023

Revised: 10 July 2023

Accepted: 11 July 2023

Published: 13 July 2023



**Copyright:** © 2023 by the authors. Licensee MDPI, Basel, Switzerland. This article is an open access article distributed under the terms and conditions of the Creative Commons Attribution (CC BY) license (<https://creativecommons.org/licenses/by/4.0/>).

## 1. Introduction

Garnet is a common mineral in skarn rocks and mainly occurs in the contact zone between intermediate-acidic intrusions and carbonate rocks. Its oscillatory zoning, compositional characteristics, and changes can reveal geological information about the hydrothermal fluids from which it formed, including the physicochemical conditions, compositional changes, and mineralization processes of the hydrothermal fluids [1–7].

The Changpo–Tongkeng tin polymetallic deposit in Dachang, Guangxi, is a world-class, superlarge, polymetallic tin deposit, with tin reserves of 0.68 million tons (average grade 1%) and zinc reserves of 4.5 million tons (average grade 4%), accompanied by copper, lead, antimony, arsenic, indium, and germanium [8]. The distribution of ore bodies in the deposit has a distinct vertical mineralization zonation feature, with skarn-type zinc–copper ore bodies located proximal to the granitic pluton in the lower part and tin polymetallic ore bodies located distal in the upper part. Among them, tin polymetallic ore bodies have been well studied, and much work has been conducted on the deposit geology, metallogenic age, diagenetic age, fluid inclusion, mineralogy, isotopic geochemistry, etc. [8–25]. However, research on the lower zinc–copper ore bodies is relatively limited.

Isotopic geochronology research shows that the metallogenic age of the tin polymetallic ore body is 95.8–90.0 Ma [10,11]; the metallogenic age of the zinc–copper ore body is 95.0 Ma [12], and these Yanshanian metallogenic ages are consistent with the diagenetic age (96.6–88.8 Ma) of the Longxianggai granitic pluton [8,13–15]. However, there are two different understandings with regard to the source of the ore-forming materials for the two types of ore bodies. After studying C, O, S, Pb, and Zn isotopes and fluid inclusions, Liang T. [8], Cai M.H. et al. [17], and Li M.Q. et al. [22,23] noted that the ore-forming fluids of zinc–copper ore bodies were mainly derived from magma, and the tin polymetallic ore bodies and zinc–copper ore bodies may have been the products of the same magmatic-hydrothermal ore-forming system. However, Zhang J. et al. [18] proposed that tin polymetallic ore bodies and zinc–copper ore bodies were not the products of the same magmatic-hydrothermal system based on fluid inclusion and Pb isotopic analyses. To further illustrate the ore-forming environment of zinc–copper ore bodies and their relationship with tin polymetallic ore bodies, we present electron probe microanalysis (EPMA) and laser ablation-inductively coupled plasma-mass spectrometry (LA-ICP-MS) analysis of garnets from the lower skarn-type zinc–copper ore bodies in the context of the geology of the deposit and garnet petrography. These data and observations are used to discuss the factors controlling the major and trace element changes in garnet and constraining the formation process and environment of garnets, thus providing a basis for understanding the metallogenic process.

## 2. Geological Setting

The Danchi metallogenic belt is located at the southwestern edge of the Jiangnan palaeoland, the junction of the Palaeo-Tethys tectonic domain and the Pacific tectonic domain. It is an important nonferrous metal metallogenic belt in China, with a length of 130 km and a width of 25 km, and it forms a narrow strip trending NW. The outcropping strata in the Danchi metallogenic belt are dominated by Devonian mudstone, marl, siliceous rocks, Carboniferous and Permian limestone, and Triassic shale. Devonian strata are the main host rocks for the tin polymetallic deposits [8,9]. Faults are widely developed, and the NW-trending Danchi and Dachang faults are the framework structures of this area. The magmatic rocks in this area are mainly intermediate-acid rocks from the late Yanshanian, and they are not often exposed to the surface. Only a small number of granite outcrops form stocks in the northern Mangchang and the central Dachang ore fields.

The Dachang ore field is located in the central part of the Danchi metallogenic belt and can be divided into three zones surrounding the central Longxianggai granite (Figure 1). The eastern zone is composed of Dafulou and Kangma tin polymetallic deposits, while the middle zone contains zinc–copper and tungsten–antimony deposits, represented by the Lamo zinc–copper deposit and the Chashan tungsten-antimony deposit; the western zone mainly includes two superlarge tin polymetallic deposits, Changpo–Tongkeng and Gaofeng [8]. The Changpo–Tongkeng deposit is the largest and most representative superlarge deposit in the Dachang ore field.

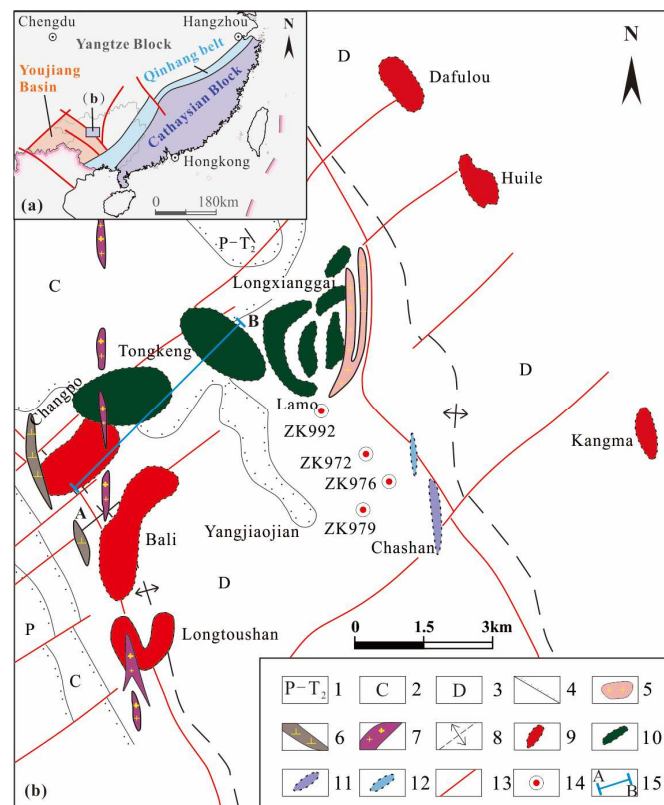


**Figure 1.** Location diagram of Dachang ore field (a) and Distribution of deposits in Dachang ore field (b); after [9]. 1. Permian-middle Triassic strata; 2. Carboniferous strata; 3. Devonian strata; 4. Unconformity boundary; 5. Biotite Granite; 6. Diorite porphyry; 7. Granite porphyry; 8. Anticlinal axis; 9. Tin ore bodies; 10. Projection of Zinc-Copper ore bodies; 11. Projection of Tungsten-Antimony ore bodies; 12. Projection of Antimony ore bodies; 13. Fault; 14. Drills; 15. Orientations and location of the profile (A,B) schematic in Figure 2.

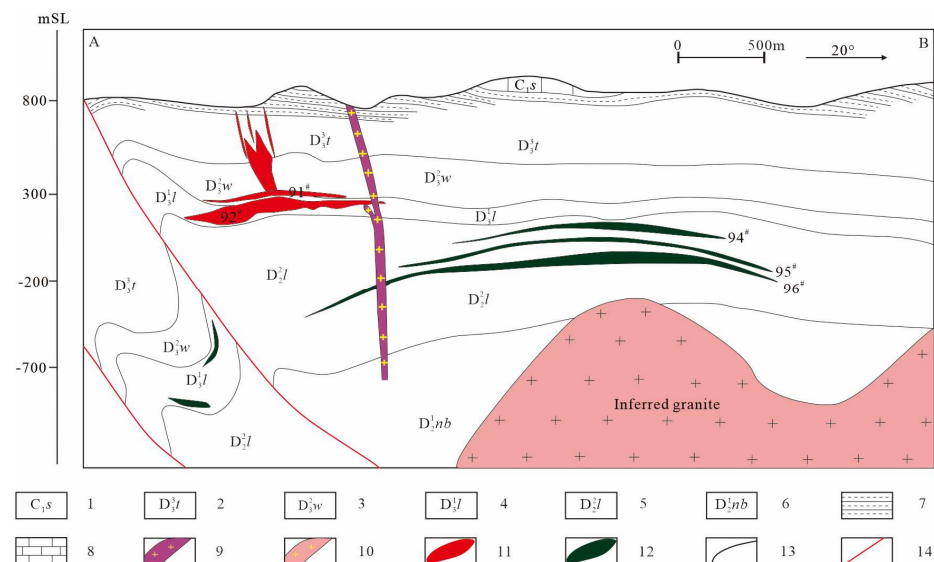


**Figure 2.** Profile of ore body distribution in the Changpo–Tongkeng deposit (After [17]), 1. Lower Carboniferous Simen Formation; 2. Upper Devonian Tongchejiang Formation; 3. Upper Devonian Wuzhishan Formation; 4. Upper Devonian Liujiang Formation; 5. Middle Devonian Luofu Formation; 6. Middle Devonian Nabiao Formation; 7. Limestone; 8. Shale; 9. Granite porphyry; 10. Inferred granite (Longxianggai granite); 11. Tin ore bodies; 12. Zinc-Copper ore bodies; 13. Stratigraphic boundary; 14. Fault.

### 3. Geology of the Deposit

The Changpo–Tongkeng tin polymetallic deposit located in the western zone of the Dachang ore field is the largest tin polymetallic deposit. The exposed strata in this area are mainly middle Devonian–lower Carboniferous clastic rocks and carbonate rocks. The lithology from bottom to top is as follows (Figure 2): the lower part of the middle Devonian Nabiao Formation ( $D_2^{1nb}$ ) mudstone and shale with reef limestone at the Longtoushan–Dachang anticline; the upper part of the middle Devonian Luofu Formation ( $D_2^l$ ) with thick stratiform limestone, black mudstone, and shale with locally lenticular carbonaceous pitch; the lower part of the upper Devonian Liujiang Formation ( $D_3^l$ ) with banded siliceous rocks containing calcareous nodules; the middle part of the upper Devonian Wuzhishan Formation ( $D_3^w$ ) limestone can be further divided into broad banded limestone ( $D_3^w^a$ ), thin banded limestone ( $D_3^w^b$ ), little bean-like limestone ( $D_3^w^c$ ), and big bean-like limestone ( $D_3^w^d$ ) from bottom to top; the upper part of the upper Devonian Tongchejiang Formation ( $D_3^t$ ) carbonate rocks and shale; and the lower Carboniferous Simen Formation ( $C_1s$ ) quartz sandstone, mudstone, and carbonaceous shale. The Devonian strata are the main host rocks of the deposit.

The structures of the deposit are complex and mainly consist of the NW-trending Dachang anticline and Dachang fault, superposed by the later NE- and SN-trending folds, faults, and fractures [8]. The Dachang anticline is an asymmetric fold with a gently dipping NE limb and a steeply dipping SW limb, and the ore bodies mainly occur on the gentle NE limb (Figure 2).

The magmatic rocks exposed in the area are Longxianggai composite granitic pluton of the late Yanshanian, which are mainly composed of medium-to-coarse-grained biotite granite, fine-grained granite, and porphyritic biotite granite, presenting a gradual spatial transition relationship. Drilling and geophysical prospecting showed that the Longxianggai granitic pluton extends to the deep part of the Changpo–Tongkeng deposit [12]. The concealed granitic pluton is located on the NE limb of the Dachang anticline, consistent with the strike of the Dachang fault. Granite porphyry dikes and diorite porphyry dikes are also found in the eastern and western part of the Changpo–Tongkeng deposit.

The ore bodies of the Changpo–Tongkeng deposit show obvious vertical mineralization zonation, with skarn-type zinc–copper ore bodies located proximal to the granitic pluton in the lower part and tin polymetallic ore bodies located distal in the upper part (Figure 2).

#### 3.1. The Upper Tin Polymetallic Ore Bodies

The tin polymetallic ore bodies are located in the upper part far from the granitic pluton, with tin reserves accounting for 80% of the Dachang ore field. In addition to high grades of tin and zinc, the ore bodies are also associated with In, Ag, As, etc. [8,19]. The ore bodies are controlled by the structures and host rock and show obvious vertical mineralization zonation. They are composed of stratiform, stratiform-like, and vein-shaped ore bodies from bottom to top. The stratiform ore bodies are the most important types in the Changpo–Tongkeng deposit, mainly composed of No. 92 and No. 91, two large ore bodies, with reserves accounting for 53% and 27% of the total tin ore reserves of the deposit, respectively. The No. 92 ore body strikes close to NW-trending, with a length of 900–1200 m and a thickness of 60–85 m. The average Sn grade is 0.8%, and that of Zn is 2.1%. The No. 91 ore body is roughly parallel to the No. 92 ore body, with a length of approximately 1000 m and an average thickness of 16 m. The average Sn grade is 1.48%, and that of Zn is 3.05%. Interlayered vein-shaped ore bodies such as No. 75, No. 77, and No. 79 are located on detachment zones at different lithological contact interfaces. The vein-shaped ore bodies can be subdivided into thin vein-shaped ore bodies and large vein-shaped ore bodies. The thin vein-shaped ore bodies are mainly composed of roughly parallel thin veins, with widths of 0.5–2 cm and lengths of 5–10 m. The average Sn grade is 1.10%, and that of Zn is 2.72%. The large vein-shaped ore bodies are located in the fractures of the Dachang reverse

anticline axis. The large vein-shaped bodies are tens to hundreds of meters long, with an average Sn content of 2.06% and an average Zn content of 8.29% [8,17].

The mineral assemblages of the upper tin polymetallic ore bodies are complex (Figure 3b,c) and include cassiterite, arsenopyrite, sphalerite, pyrite, jamesonite, pyrrhotite, tetrahedrite, chalcopyrite, and galena. The gangue minerals are mainly quartz, calcite, and tourmaline. The ore bodies are massive, banded, lenticular, disseminated, and form stockworks. Metasomatic, zonation, emulsion, euhedral granular, and subhedral–anhedral are some of the textures identified.

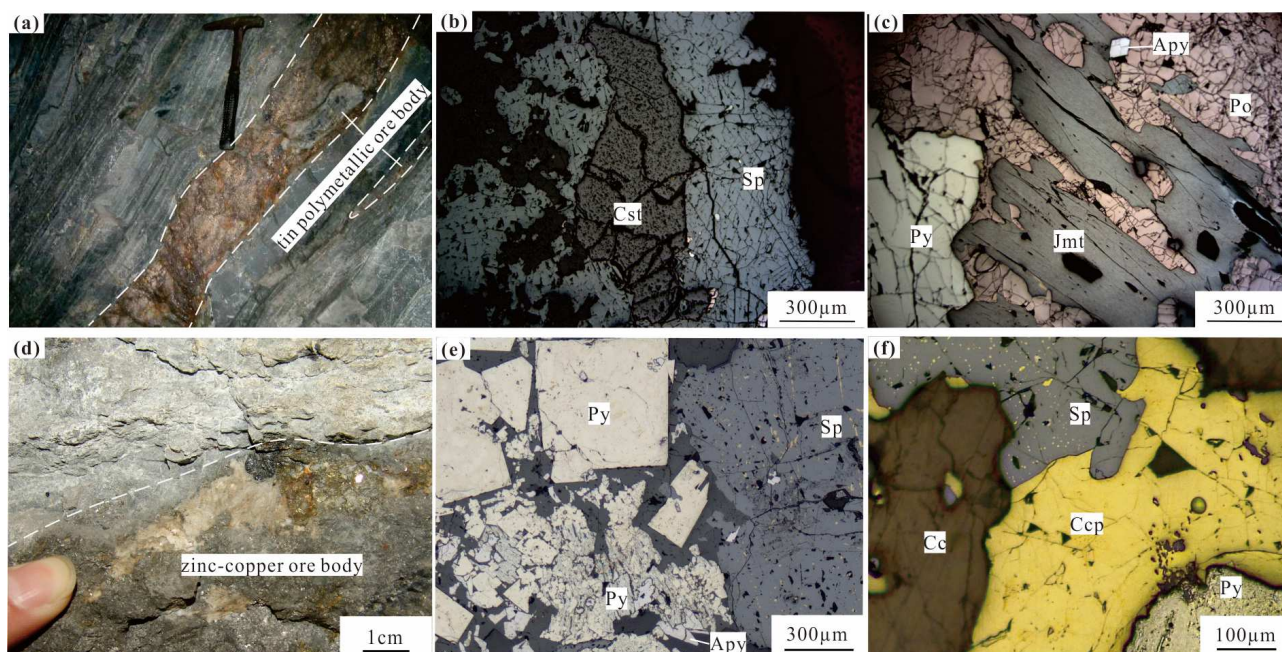


**Figure 3.** Characteristics of ore parageneses in Changpo–Tongkeng deposit. (a) No. 92 stratiform tin polymetallic ore body; (b) Cassiterite and sphalerite in No. 92 ore body; (c) Pyrrhotite, pyrite, arsenopyrite, and jamesonite in No. 92 ore body; (d) Stratiform zinc–copper ore body; (e) Pyrite, arsenopyrite, and sphalerite in zinc–copper ore body; (f) Pyrite, sphalerite, and chalcopyrite in zinc–copper ore body. (a–c) Tin polymetallic ore body; (d–f) Zinc–copper ore body. Mineral abbreviations: Py—pyrite; Apy—arsenopyrite; Sp—sphalerite; Ccp—chalcopyrite; Cst—cassiterite; Jmt—jamesonite; Po—Pyrrhotite; Cc—calcite.

### 3.2. The Lower Zinc–Copper Ore Bodies

The zinc–copper ore bodies are located in the contact zone between the granitic pluton and the calcareous mudstone and marl of the Middle Devonian Luofu Formation ( $D_2^l$ ) and mainly consist of three roughly parallel stratiform ore bodies, No. 96, No. 95, and No. 94 (Figure 2). The ore bodies strike  $58\text{--}65^\circ$ , dipping  $21\text{--}28^\circ$ , with total Zn reserves of 2.1 million tons, total Cu reserves of 80,000 tons, and total Ag reserves of 849 tons [17]. The Zn metal content in the No. 96 ore body exceeds 1 million tons, with a strike length of 2235 m and an average thickness of 8.74 m. The average Zn grade is 5.92%, that of Cu is 0.22%, and that of Ag is 25.64 g/t. The No. 95 ore body is approximately 1500 m along the strike, with a thickness of 0.66–31.76 m. The average Zn grade is 2.76%, that of Cu is 0.38%, that of Pb is 0.11%, and that of Sb is 0.02%. The No. 94 ore body extends approximately 2595 m along the strike, with a thickness of 0.52–20 m. The average Zn grade is 3.1%, that of Cu is 0.14%, that of Pb is 0.29%, and that of Sb is 0.06%.

The mineral paragenesis of the zinc–copper ore body is sphalerite, chalcopyrite, arsenopyrite, pyrrhotite, and pyrite (Figure 3e,f). The gangue minerals are mainly garnet, vesuvianite, diopside, wollastonite, actinolite, chlorite, epidote, axinite, fluorite, calcite,

and quartz (Figure 4). Massive and disseminated structures prevail, forming metasomatic, subhedral–anhedral, zoning, and emulsion textures.

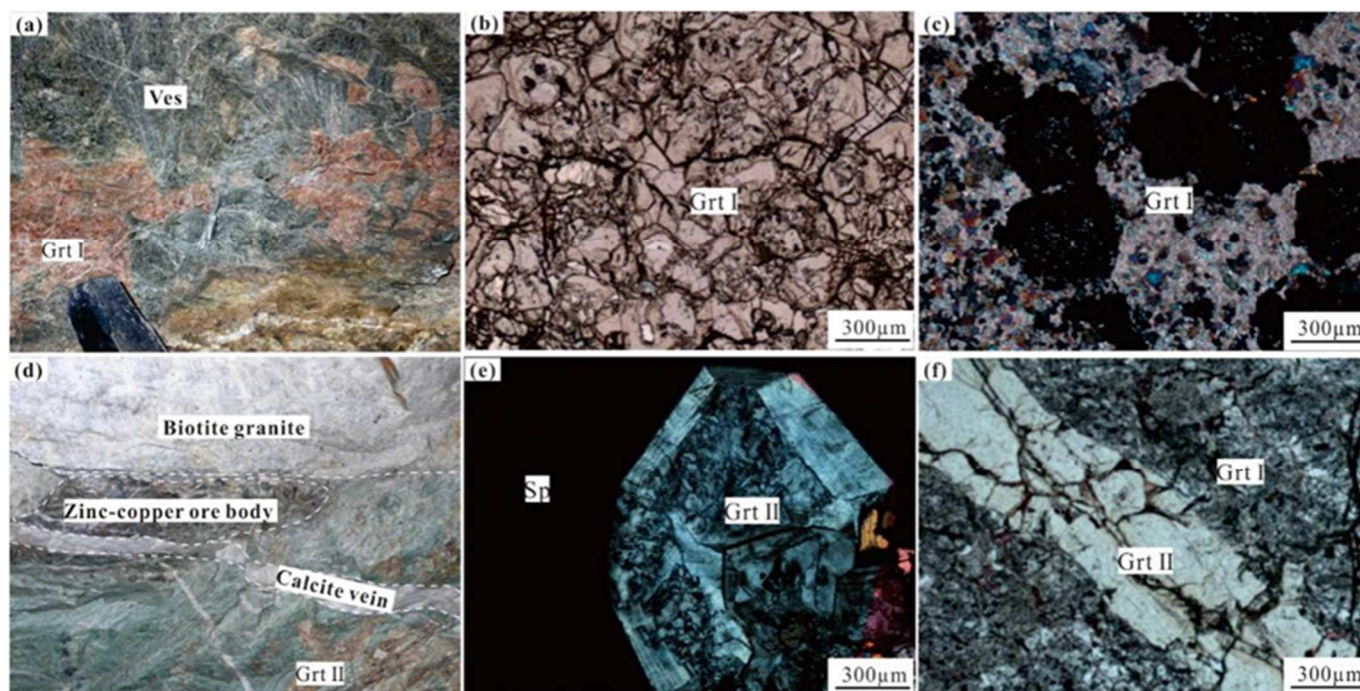


**Figure 4.** Photos of garnet in the Changpo–Tongkeng deposit. (a) Macroscopic image of Grt I intergrows with vesuvianite; (b) Plain polarized image of Grt I presents a euhedral–subhedral granular with a rough surface and a dissolution texture; (c) Crossed polarized image of homogeneous Grt I; (d) Macroscopic image of Grt II related to Zn–Cu mineralization; (e) Crossed polarized image of Grt II intergrows with sphalerite; (f) Plain polarized image of Grt I cut by vein Grt II. Mineral abbreviations: Grt I—early generation garnet; Ves—vesuvianite; Grt II—late generation garnet; Sp—sphalerite.

The intrusion of granitic pluton causes the metamorphism of the host rock, which forms skarn and hornfels. Based on the mineralogical features, skarn can be divided into two stages. The early stage is ore-free, while the late stage of skarn is associated with ore (Figure 4a,d). In the early stage, garnet, diopside, wollastonite, and vesuvianite are formed, while in the late stage, aqueous silicate minerals such as actinolite, axinite, chlorite, and epidote are formed.

According to the spatial distribution, occurrence characteristics, and ore mineralogy, the mineralization at the Changpo–Tongkeng tin polymetallic deposit can be divided into two periods and five stages. The first is the skarn zinc–copper mineralization period (I), which can be divided into skarnization (I<sub>1</sub>) and sulfide stages (I<sub>2</sub>). The second is the cassiterite–sulfide mineralization period (II), which can be divided into three stages: cassiterite–sulfide–tourmaline–quartz stage (II<sub>1</sub>), cassiterite–sulfide–sulfosalt–quartz stage (II<sub>2</sub>), and sulfide–sulfosalt–quartz–calcite stage (II<sub>3</sub>).

#### 4. Sampling and Analytical Methods

The samples were collected from the lower zinc–copper ore bodies of the Changpo–Tongkeng deposit, with garnet, diopside, vesuvianite, axinite, calcite, and sphalerite. Based on field geological surveys and microscopic observations, representative garnet samples were selected for major and trace elemental content analysis using EPMA and LA-ICP-MS, respectively.

Major elemental compositions were determined by EPMA at the Laboratory of Mineralization and Dynamics, Chang’an University, Xi’an, China, using a JXA-iHP200F with an acceleration voltage of 15 kV, a beam current of 10 nA, and a beam spot diameter of 1 µm.

In situ trace element analysis was performed by LA-ICP-MS at the Laboratory of Mineralization and Dynamics, Chang'an University, Xi'an, China. Analyses were conducted using a Photon Machines Analyte Excite 193 laser ablation system coupled with an Agilent 7900 Quadrupole ICP-MS. Helium was used as the carrier gas with a flow rate of 0.5 L/min, and argon was used as the make-up gas with a flow rate of 0.8 L/min. The beam spot diameter was 35  $\mu\text{m}$ , with a 6.4 J/cm<sup>2</sup> energy density and 11 Hz repetition rate. Each analysis included 25 s of background measurement and 40 s of data acquisition. The NIST610 glass standard was used for external calibration. The trace elements analyzed included Sn, B, Cl, Sc, V, Cr, Co, Ni, Cu, Zn, Ga, Ge, Rb, Sr, Y, Zr, Nb, Mo, Cd, In, Sb, Cs, Ba, La, Ce, Pr, Nd, Sm, Eu, Gd, Tb, Dy, Ho, Er, Tm, Yb, Lu, Hf, Ta, W, Tl, Pb, Th, U, and As. Off-line data processing was performed using ICPMSDataCal software.

## 5. Results

### 5.1. Petrography Characteristics

The garnets in hand specimens showed a light brownish-red color (Figure 4a,d), with euhedral–subhedral texture and grain sizes ranging from 0.6 to 5 mm. Under the microscope, the garnets were colorless to light brown. Based on the hand specimens and microscopic observations, the garnets could be divided into two generations: an early generation (Grt I) and a late generation (Grt II). Grt I displayed a euhedral–subhedral pentagonal dodecahedron texture, with a dissolution texture, and the surface of Grt I was rough. It exhibited homogeneous or local abnormal extinction, lacked well-developed zoning (Figure 4b,c), and often intergrew with wollastonite, vesuvianite, diopside, etc. (Figure 4a). Grt II was associated with sulfides or cuts through Grt I in a vein-like pattern (Figure 4e,f), with a euhedral–subhedral texture and obvious heterogeneity. Grt II also showed well-developed zoning.

### 5.2. EPMA Analysis Results

The EPMA analysis results for the two generations of garnet are given in Table 1. For Grt I, the SiO<sub>2</sub> content ranged from 37.44 to 39.31 wt% (avg. 38.43 wt%); the CaO content ranged from 34.43 to 35.84 wt% (avg. 35.25 wt%); the Al<sub>2</sub>O<sub>3</sub> content ranged from 10.47 to 19.08 wt% (avg. 17.12 wt%); the FeO<sup>T</sup> content ranged from 4.97 to 15.54 wt% (avg. 7.45 wt%); and the MnO content ranged from 0.60 to 1.45 wt% (avg. 0.92 wt%) (Figure 5). The data (based on 12 oxygen atoms) showed that Grt I was Al-rich and dominated by grossular (And<sub>12–50</sub>Gro<sub>46–82</sub>, avg. And<sub>25</sub>Gro<sub>72</sub>; Table 1, Figure 6).

**Table 1.** Major element compositions (wt%) of the garnets.

Sample	1511-5-1 (N = 4)			1511-19-1 (N = 5)			1511-19-2 (N = 5)			1511-19-3 (N = 3)			1511-8-1
	Max.	Min.	Avg.	Max.	Min.	Avg.	Max.	Min.	Avg.	Max.	Min.	Avg.	Max.
Generation	Grt I												
SiO <sub>2</sub>	38.11	37.44	37.81	39.11	38.25	38.72	38.95	38.37	38.62	39.31	38.25	38.67	38.94
TiO <sub>2</sub>	0.74	0.16	0.43	0.39	0.24	0.3	0.73	0.01	0.55	0.74	0.24	0.56	0.13
Al <sub>2</sub> O <sub>3</sub>	15.86	10.47	14.08	18.98	17.94	18.68	19	18.47	18.76	19.08	17.13	18.36	16.39
Cr <sub>2</sub> O <sub>3</sub>	b.d.l.	b.d.l.	b.d.l.	0.14	b.d.l.	0.04	0.09	b.d.l.	0.04	0.08	0.02	0.05	0.05
FeO	15.54	8.1	10.59	6.9	5.4	6	6.17	5.47	5.78	7.22	4.97	5.74	9.33
MnO	0.97	0.66	0.79	1.23	0.66	0.84	0.89	0.6	0.73	1.45	0.6	0.91	1.22
MgO	0.04	0.01	0.02	0.04	0.02	0.03	0.07	0.03	0.04	0.05	0.04	0.05	0.07
CaO	35.81	34.46	35.35	35.76	35.1	35.51	35.79	35.09	35.44	35.84	34.74	35.43	35.44
Na <sub>2</sub> O	0.01	b.d.l.	b.d.l.	0.01	b.d.l.	b.d.l.	0.01	b.d.l.	b.d.l.	0.01	b.d.l.	0.01	0.02
K <sub>2</sub> O	b.d.l.	b.d.l.	b.d.l.	0.02	b.d.l.	0.01	0.01	b.d.l.	b.d.l.	0.01	b.d.l.	0.01	0.04
SnO <sub>2</sub>	0.2	0.07	0.11	0.05	b.d.l.	0.03	0.06	b.d.l.	0.02	0.02	b.d.l.	0.01	0.08
Total	99.71	98.91	99.2	100.57	99.73	100.15	100.46	99.46	99.99	100.57	99.38	99.79	100.94
Spe	2.11	1.45	1.74	2.67	1.42	1.81	1.9	1.29	1.57	3.16	1.28	1.97	2.69
And	50.2	31.45	38.4	22.42	15.53	18.94	21.04	12.9	17.15	22.9	12.25	17.71	30.15
Gro	66.93	46.47	59.69	81.25	73.64	77.66	80.89	75.26	79.06	81.75	72.79	78.15	70

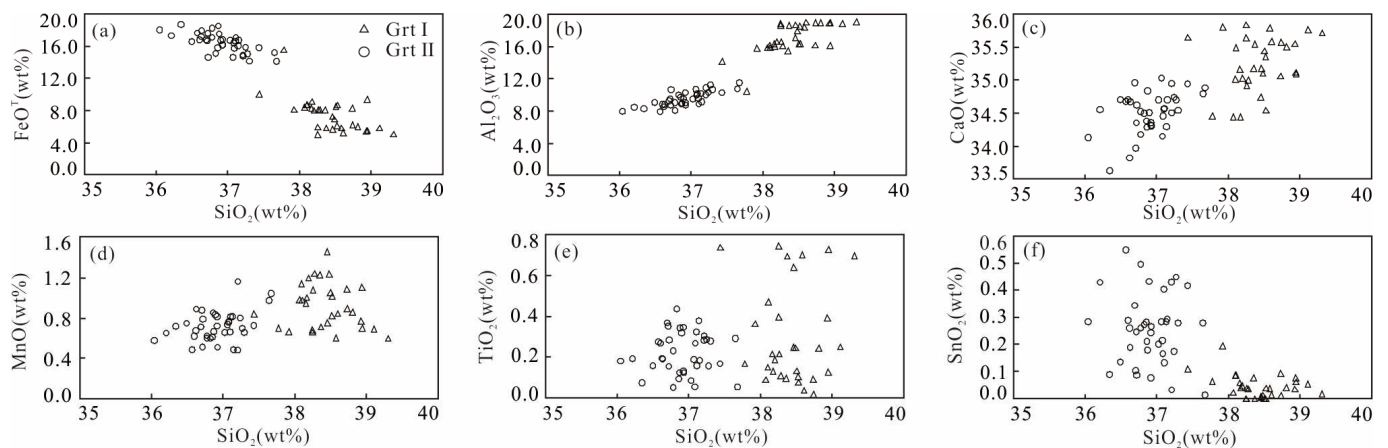
**Table 1.** Cont.

Sample	1511-8-1 (N = 4)	1511-8-2 (N = 5)			1511-8-3 (N = 5)			1511-6-1 (N = 9)			1511-6-2 (N = 6)		
	Min.	Avg.	Max.	Min.	Avg.	Max.	Min.	Avg.	Max.	Min.	Avg.	Max.	Min.
Generation		Grt I						Grt II					
SiO <sub>2</sub>	38.36	38.58	38.61	38.07	38.24	38.73	38.16	38.37	37.65	36.71	37.15	37.3	36.72
TiO <sub>2</sub>	0.07	0.1	0.15	0.03	0.1	0.21	0.09	0.16	0.35	0.12	0.25	0.37	0.26
Al <sub>2</sub> O <sub>3</sub>	15.52	16.11	19.05	15.86	16.64	18.55	16.21	16.88	11.25	8.86	10.02	10.89	9.04
Cr <sub>2</sub> O <sub>3</sub>	b.d.l.	0.01	0.07	b.d.l.	0.02	0.13	b.d.l.	0.04	0.13	b.d.l.	0.04	0.08	b.d.l.
FeO	8.03	8.61	9.09	5.2	7.87	8.31	6.05	7.75	18.49	14.9	16.13	16.15	14.13
MnO	1.01	1.1	1.23	0.84	1.04	1.19	0.82	1.02	0.97	0.48	0.76	1.16	0.66
MgO	0.03	0.05	0.07	0.03	0.06	0.08	0.04	0.05	0.04	0.01	0.03	0.03	0.01
CaO	34.54	35.07	35.59	34.43	34.89	35.35	34.92	35.1	34.95	33.96	34.6	34.62	34.29
Na <sub>2</sub> O	b.d.l.	0.01	0.01	b.d.l.	b.d.l.	0.02	b.d.l.	b.d.l.	b.d.l.	b.d.l.	b.d.l.	0.01	b.d.l.
K <sub>2</sub> O	b.d.l.	0.01	b.d.l.	b.d.l.	b.d.l.	0.01	b.d.l.	b.d.l.	0.01	b.d.l.	b.d.l.	0.02	b.d.l.
SnO <sub>2</sub>	b.d.l.	0.05	0.09	0.02	0.04	0.09	b.d.l.	0.05	0.45	0.1	0.32	0.29	0.03
Total	98.52	99.71	99.47	97.87	98.9	99.63	99.3	99.43	99.97	98.25	99.3	99.14	97.74
Spe	2.22	2.39	2.71	1.82	2.28	2.6	1.77	2.23	2.15	1.09	1.71	2.58	1.49
And	25.57	28.29	31.08	18.68	26.48	28.73	20.27	25.86	65.76	52.12	56.95	57.4	48.4
Gro	66.85	68.35	78.46	65.27	70.15	76.06	68.25	70.82	45.85	31.05	40.94	49.34	41.45

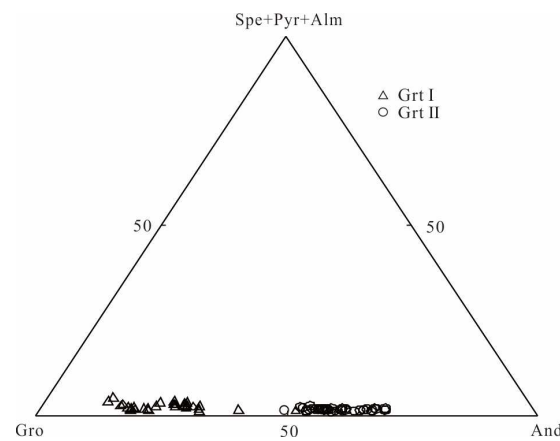
  

Sample	1511-6-2	1507-20-1 (N = 5)			1507-20-2 (N = 5)			1507-20-3 (N = 6)			1507-20-4 (N = 7)		
	Avg.	Max.	Min.	Avg.	Max.	Min.	Avg.	Max.	Min.	Avg.	Max.	Min.	Avg.
Generation		Grt II											
SiO <sub>2</sub>	37.06	37.08	36.69	36.94	37.15	36.57	36.83	37.68	36.34	36.86	36.92	36.04	36.56
TiO <sub>2</sub>	0.31	0.36	0.05	0.15	0.34	0.05	0.21	0.19	0.05	0.12	0.43	0.13	0.22
Al <sub>2</sub> O <sub>3</sub>	10.27	10.71	9.26	9.83	9.14	7.91	8.62	11.53	8.3	9.17	10.29	7.97	9.01
Cr <sub>2</sub> O <sub>3</sub>	0.03	0.12	b.d.l.	0.03	0.12	b.d.l.	0.06	0.1	b.d.l.	0.05	0.14	b.d.l.	0.04
FeO	15.23	16.78	14.59	16.05	18.23	16.72	17.43	18.67	14.1	16.73	18.01	15.09	16.97
MnO	0.83	0.76	0.61	0.69	0.66	0.48	0.57	1.04	0.51	0.75	0.89	0.51	0.65
MgO	0.02	0.03	0.02	0.02	0.05	0.01	0.02	0.05	0.02	0.03	0.06	0.02	0.04
CaO	34.46	35.03	34.14	34.64	34.84	34.17	34.58	34.88	33.62	34.31	34.7	34.12	34.46
Na <sub>2</sub> O	b.d.l.	b.d.l.	b.d.l.	b.d.l.	0.02	b.d.l.	b.d.l.	0.02	0.01	0.01	0.01	b.d.l.	b.d.l.
K <sub>2</sub> O	0.01	0.01	b.d.l.	0.01	0.01	b.d.l.	b.d.l.	0.04	b.d.l.	0.02	0.02	b.d.l.	0.01
SnO <sub>2</sub>	0.16	0.35	0.2	0.27	0.55	0.18	0.36	0.27	0.01	0.15	0.43	0.19	0.28
Total	98.36	99.24	97.77	98.64	99.44	97.99	98.68	99.4	97.39	98.2	99.32	97.26	98.23
Spe	1.87	1.71	1.39	1.56	1.48	1.1	1.29	2.29	1.16	1.69	1.97	1.16	1.47
And	53.93	64.6	56.02	58.96	66.68	58.54	63.22	66.17	51.52	60.54	69.06	53.65	63.41
Gro	44.02	42.69	33.65	39.37	40.62	32.07	35.41	45.9	30.69	37.5	45.48	29.24	34.98

Note: b.d.l.—below detection limit.



**Figure 5.** Plots of SiO<sub>2</sub> contents vs. FeO<sup>T</sup> (a), Al<sub>2</sub>O<sub>3</sub> (b), CaO (c), MnO (d), TiO<sub>2</sub> (e) and SnO<sub>2</sub> (f) contents of the garnets.



**Figure 6.** Triangular classification diagram of the garnets. Endmember abbreviations: And—andradite; Gro—grossular; Spe—spessartine; Pyr—pyrope; Alm—almandine.

For Grt II, the SiO<sub>2</sub> content ranged from 36.04 to 37.68 wt% (avg. 36.91 wt%); the CaO content ranged from 33.62 to 35.03 wt% (avg. 34.51 wt%); the Al<sub>2</sub>O<sub>3</sub> content ranged from 7.91 to 11.53 wt% (avg. 9.53 wt%); the FeO<sup>T</sup> content ranged from 14.10 to 18.67 wt% (avg. 16.40 wt%); and the MnO content ranged from 0.48 to 1.16 wt% (avg. 0.72 wt%) (Figure 5). The data (based on 12 oxygen atoms) showed that Grt II was Fe-rich and dominated by andradite (And<sub>48–69</sub>Gro<sub>29–49</sub>, avg. And<sub>59</sub>Gro<sub>39</sub>; Table 1, Figure 6).

Grt I lacked well-developed zoning (Figure 7a), and it showed homogeneity from the core to the rim, with little variation in element content (Figure 7b). Grt II had significant heterogeneity and well-developed oscillatory zoning (Figure 7c). From the core to the rim, the CaO content showed limited variation, while the FeO<sup>T</sup> content increased and the Al<sub>2</sub>O<sub>3</sub> content decreased. The variations in endmember compositions of andradite and grossular were consistent with the contents of FeO<sup>T</sup> and Al<sub>2</sub>O<sub>3</sub> (Figure 7d).

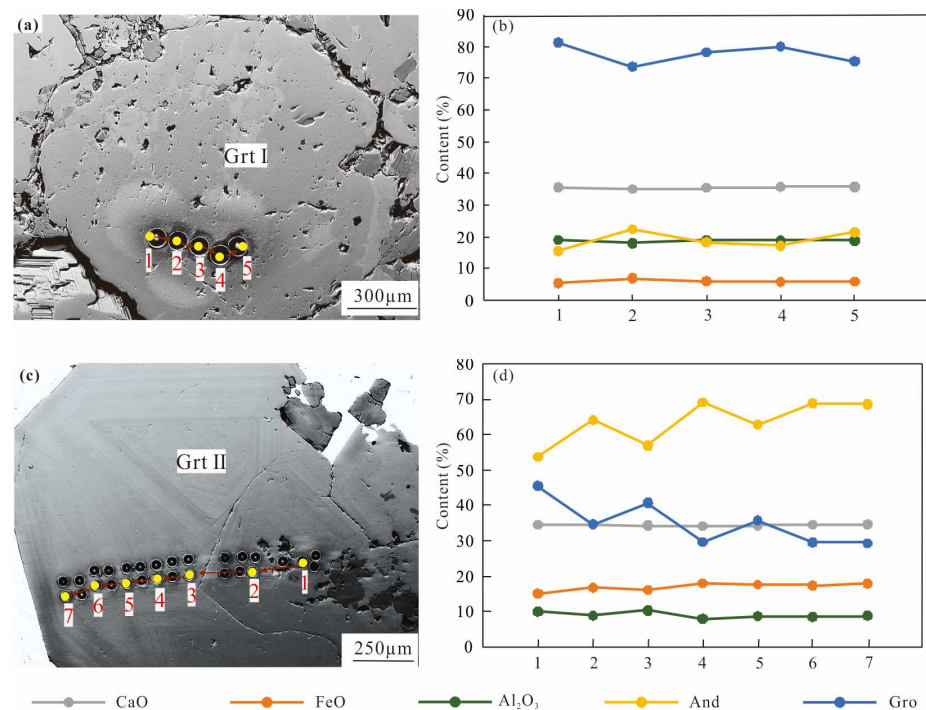


**Figure 7.** Composition and endmember variation diagrams of representative garnets. (a) EPMA analytical points of Grt I; (b) Element content and endmember composition of Grt I; (c) EPMA analytical points of Grt II; (d) Element content and endmember composition of Grt II.

The EPMA analysis results showed that the garnets contained a small amount of SnO<sub>2</sub>, with that for Grt I ranging from below detection limit to 0.20 wt% (avg. 0.04 wt%) and that for Grt II ranging from 0.01 to 0.55 wt% (avg. 0.26 wt%). The SnO<sub>2</sub> content in Grt II was significantly higher than that in Grt I.

### 5.3. LA-ICP-MS Analysis Results

The LA-ICP-MS analysis results of the two garnet generations are given in Table 2. All garnets were strongly depleted in large ion lithophile elements (LILEs) compared to the primitive mantle [26], with the contents of elements such as Rb, Cs, Ba, and K below the detection limit. Grt I had 1.08–1.72 ppm Hf (avg. 1.50 ppm), 15.54–30.39 ppm Zr (avg. 23.65 ppm), 2.51–6.15 ppm Nb (avg. 4.66 ppm), and 0.12–0.83 ppm Ta (avg. 0.36 ppm). Grt II had 0.62–2.48 ppm Hf (avg. 1.62 ppm), 42.41–101.13 ppm Zr (avg. 68.58 ppm), 0.45–7.96 ppm Nb (avg. 4.90 ppm), 0.02–0.69 ppm Ta (avg. 0.32 ppm), 0.05–0.76 ppm Th (avg. 0.20 ppm), and 0.19–0.84 ppm U (avg. 0.34 ppm).

**Table 2.** Trace element compositions (ppm) of the garnets.

Sample	1511-19-1 (N = 5)			1511-19-2 (N = 5)			1511-6-1 (N = 15)			1507-20-4 (N = 28)		
	Max.	Min.	Avg.	Max.	Min.	Avg.	Max.	Min.	Avg.	Max.	Min.	Avg.
Generation	Grt I						Grt II					
Sn	372.42	340.11	357.02	539.05	466.19	521.02	4137.47	2051.14	2828.50	3953.07	2051.14	2650.02
B	15.45	7.74	9.87	12.67	7.99	9.98	19.75	9.64	13.70	17.57	9.64	13.45
Cl	483.37	b.d.l.	244.25	b.d.l.	b.d.l.	b.d.l.	407.85	b.d.l.	130.67	407.85	b.d.l.	170.51
Sc	13.27	7.59	9.37	9.38	5.39	6.85	66.78	4.82	17.99	66.78	4.82	26.49
V	316.24	225.44	278.01	287.26	179.29	217.36	505.70	71.29	198.87	505.70	71.29	276.57
Cr	20.20	10.08	14.02	36.08	19.56	25.17	674.07	b.d.l.	92.07	674.07	15.36	140.35
Zn	9.14	6.96	7.86	10.04	8.21	8.93	16.50	1.95	3.29	16.50	1.95	3.22
Ga	32.47	30.27	31.68	31.52	30.12	30.58	43.08	20.26	26.27	26.71	20.26	22.66
Ge	4.65	2.60	3.35	4.10	2.56	3.09	23.60	4.24	10.00	10.62	4.24	7.68
As	b.d.l.	b.d.l.	b.d.l.	0.71	b.d.l.	0.14	6.31	b.d.l.	0.92	6.31	b.d.l.	1.21
Sr	0.12	0.03	0.08	0.12	0.02	0.07	0.53	b.d.l.	0.07	0.53	b.d.l.	0.07
Zr	20.61	15.54	18.20	30.39	26.48	29.10	101.13	42.41	68.58	101.13	42.41	75.99
Nb	5.20	2.51	3.88	6.15	4.33	5.43	7.96	0.45	4.90	7.96	0.45	4.27
In	2.09	1.80	1.94	2.59	2.43	2.53	46.80	13.04	22.84	20.75	13.04	15.68
Sb	b.d.l.	b.d.l.	b.d.l.	b.d.l.	b.d.l.	b.d.l.	0.45	b.d.l.	0.16	0.38	b.d.l.	0.15
Hf	1.69	1.08	1.35	1.72	1.60	1.65	2.48	0.62	1.62	2.48	0.62	1.89
Ta	0.83	0.12	0.43	0.38	0.22	0.29	0.69	0.02	0.32	0.51	0.02	0.25
W	0.21	0.17	0.19	0.44	0.33	0.39	12.81	3.05	7.36	12.81	3.05	8.06
Th	b.d.l.	b.d.l.	b.d.l.	b.d.l.	b.d.l.	b.d.l.	0.76	0.05	0.20	0.76	0.05	0.29
U	0.01	b.d.l.	b.d.l.	0.003	b.d.l.	b.d.l.	0.84	0.19	0.34	0.84	0.19	0.39
La	0.003	b.d.l.	b.d.l.	0.01	b.d.l.	b.d.l.	0.22	0.02	0.04	0.22	0.02	0.05
Ce	0.01	b.d.l.	0.01	0.02	0.01	0.01	1.11	0.32	0.49	1.11	0.32	0.61
Pr	0.01	b.d.l.	b.d.l.	0.01	b.d.l.	0.01	0.74	0.19	0.32	0.74	b.d.l.	0.39
Nd	0.11	0.01	0.07	0.11	0.04	0.07	9.69	3.00	4.49	9.69	3.00	5.31
Sm	0.10	b.d.l.	0.06	0.13	0.05	0.10	7.73	2.66	4.17	7.73	2.66	4.57
Eu	0.06	0.02	0.04	0.07	b.d.l.	0.04	0.67	0.32	0.44	0.67	0.32	0.49
Gd	0.32	0.22	0.27	0.50	0.39	0.44	11.29	3.74	6.78	11.29	3.74	7.53
Tb	0.13	0.08	0.10	0.15	0.12	0.13	1.82	0.56	1.14	1.82	0.56	1.31
Dy	1.44	1.10	1.29	1.66	1.39	1.51	13.09	3.15	7.55	13.09	3.15	9.02
Ho	0.47	0.39	0.43	0.51	0.41	0.46	3.35	0.65	1.58	3.35	0.65	1.97
Er	2.12	1.43	1.69	1.88	1.62	1.75	10.51	1.70	4.40	10.51	1.70	5.55
Tm	0.37	0.28	0.32	0.30	0.25	0.28	1.47	0.18	0.55	1.47	0.18	0.70
Yb	2.80	1.95	2.33	2.24	1.85	2.05	8.69	1.14	3.20	8.69	1.14	4.05
Lu	0.46	0.33	0.37	0.34	0.25	0.29	1.12	0.16	0.43	1.12	0.16	0.54
Y	15.91	13.04	14.44	15.83	14.89	15.22	130.60	23.65	57.59	130.60	23.65	71.53

Table 2. Cont.

Sample	1511-19-1 (N = 5)			1511-19-2 (N = 5)			1511-6-1 (N = 15)			1507-20-4 (N = 28)		
	Max.	Min.	Avg.	Max.	Min.	Avg.	Max.	Min.	Avg.	Max.	Min.	Avg.
Generation	Grt I						Grt II					
ΣREE	8.01	6.02	6.98	7.53	6.78	7.13	59.30	18.84	35.58	59.30	18.84	42.08
LREE	0.25	0.10	0.18	0.27	0.17	0.22	19.94	7.14	9.95	19.94	7.14	11.42
HREE	7.91	5.84	6.81	7.26	6.62	6.91	48.82	11.29	25.63	48.82	11.29	30.66
LREE/HREE	0.03	0.01	0.02	0.04	0.03	0.03	0.67	0.17	0.41	0.67	0.17	0.40
δEu	0.94	0.47	0.67	0.89	b.d.l.	0.58	0.29	0.18	0.24	0.44	0.18	0.26
δCe	0.62	0.50	0.57	0.71	0.24	0.50	0.49	0.32	0.40	0.55	0.40	0.47

Note: b.d.l.—below detection limit.

Both generations of garnet contained ore-forming elements and trace elements, including W, Sn, As, In, Ge, and Ga. For Grt I, the contents of W ranged from 0.17 to 0.44 ppm (avg. 0.29 ppm); the Sn content ranged from 340.11 to 539.05 ppm (avg. 439.02 ppm); the As content ranged from below detection limit to 0.71 ppm (avg. 0.07 ppm); the In content ranged from 1.80 to 2.59 ppm (avg. 2.24 ppm); the Ge content ranged from 2.56 to 4.65 ppm (avg. 3.22 ppm); and the Ga content ranged from 30.12 to 32.47 ppm (avg. 31.13 ppm). For Grt II, the W content ranged from 3.05 to 12.81 ppm (avg. 7.36 ppm); the Sn content ranged from 2051.14 to 4137.47 ppm (avg. 2828.50 ppm); the As content ranged from 0.57 to 6.31 ppm (avg. 0.92 ppm); the In content ranged from 13.04 to 46.80 ppm (avg. 22.84 ppm); the Ge content ranged from 4.24 to 23.60 ppm (avg. 10.00 ppm); and the Ga content ranged from 20.26 to 43.08 ppm (avg. 26.27 ppm). The concentrations of W, Sn, As, In, and Ge in Grt II were higher than those in Grt I, while the Ga content was lower than that in Grt I (Figure 8).

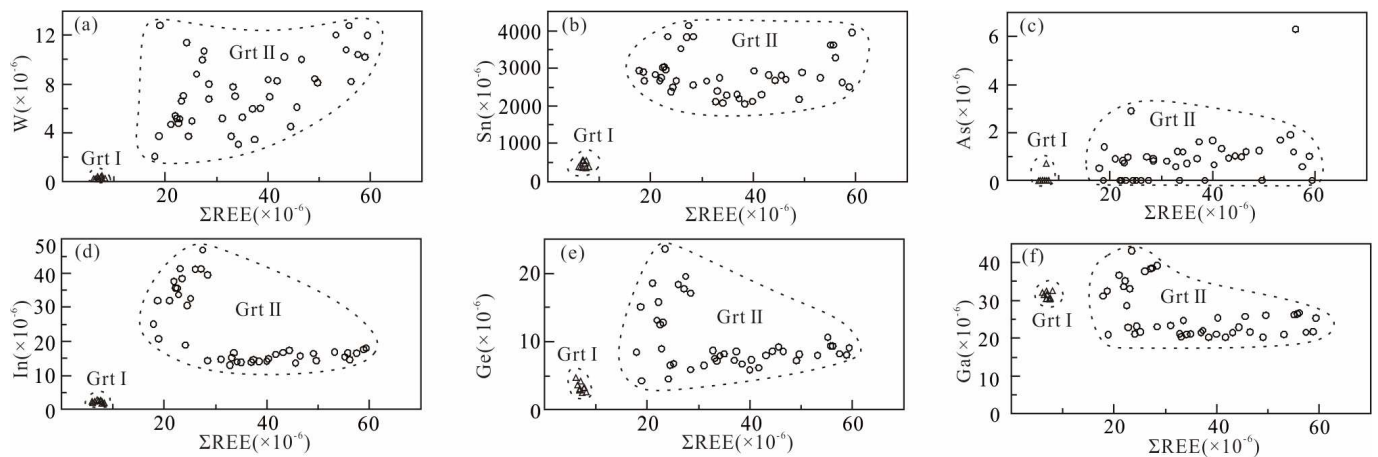
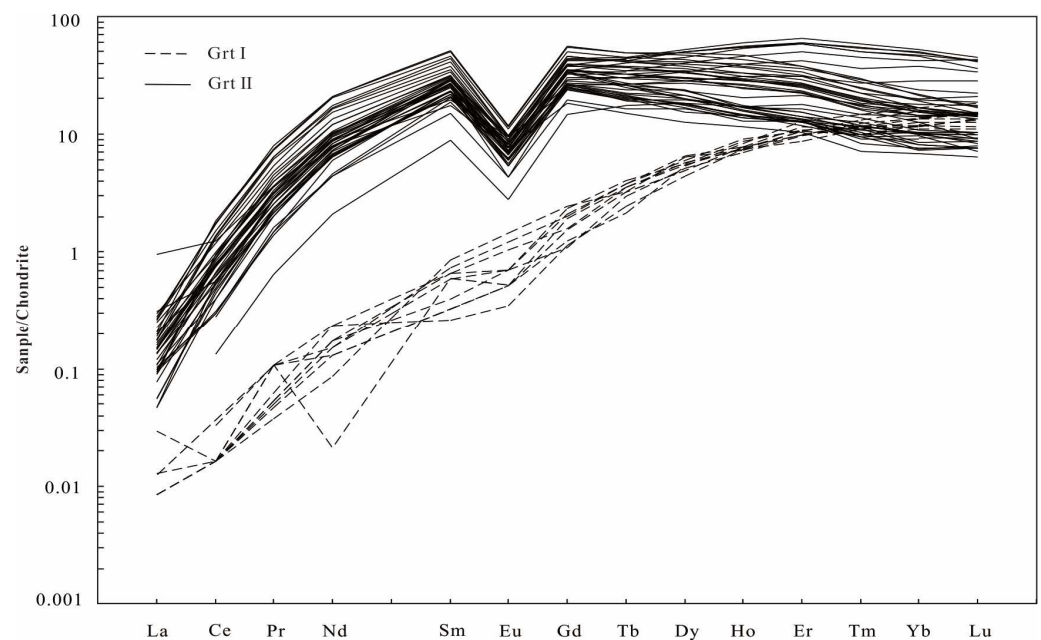


Figure 8. Plots of ΣREE content vs. W (a), Sn (b), As (c), In (d), Ge (e), and Ga (f) contents of the garnets.

Both generations of garnet showed significant depletion in light rare earth elements (LREEs) and enrichment in heavy rare earth elements (HREEs; Figure 9). For Grt I, the total rare earth element (ΣREE) content ranged from 6.02 to 8.01 ppm (avg. 7.06 ppm); the ΣLREE/ΣHREE ratio ranged from 0.01 to 0.04, with weakly negative or no evident Eu anomalies (δEu = 0.47–0.94, avg. 0.67). For Grt II, the ΣREE content ranged from 18.84 to 59.3 ppm (avg. 35.88 ppm); the ΣLREE/ΣHREE ratio ranged from 0.17 to 0.67, with a pronounced negative Eu anomaly (δEu = 0.18–0.44, avg. 0.26). The ΣREE content and ΣLREE/ΣHREE ratio of Grt II were higher than those of Grt I, while δEu was lower than that of Grt I.



**Figure 9.** Chondrite-normalized REE patterns of the garnets (normalization values after [26]).

## 6. Discussion

### 6.1. Composition of REEs in Garnet and Its Significance

The chemical formula of garnet is  $X_3Y_2[SiO_4]_3$ , where X represents divalent cations (such as  $Ca^{2+}$ ,  $Mn^{2+}$ ,  $Mg^{2+}$ , or  $Fe^{2+}$ ) in the dodecahedral site and Y represents trivalent cations (such as  $Fe^{3+}$ ,  $Al^{3+}$ , or  $Cr^{3+}$ ) in the octahedral site [27,28]. Incorporation of trace elements, including REEs, into garnet crystals can occur in four ways: surface adsorption, occlusion, isomorphous substitution, and interstitial solid solution [29]. The first two are mainly influenced by kinetic factors during crystal growth, while the latter two are controlled by crystal chemistry [5,30].

Limited by ionic radius,  $REE^{3+}$  can only occupy octahedral positions to substitute for  $X^{2+}$  through isomorphous substitution [1,5,31,32]. Possible isomorphous substitution mechanisms include the following: 1.  $REE^{3+} + X^{2+} \leftrightarrow 2Ca^{2+}$  [33,34]; 2.  $REE^{3+} + Z^{3+} \leftrightarrow Ca^{2+} + Si^{4+}$  [4,29,30]; 3.  $REE^{3+} + Y^{2+} \leftrightarrow Ca^{2+} + Y^{3+}$  [35–37]; and 4.  $2REE^{3+} + \square \leftrightarrow 3Ca^{2+}$  [38,39], where  $X^{2+}$  represents  $Na^{+}$ ;  $Z^{3+}$  is generally  $Al^{3+}$  and  $Fe^{3+}$ ;  $Y^{2+}$  is generally  $Mg^{2+}$ ,  $Fe^{2+}$ ;  $Y^{3+}$  mainly represents  $Al^{3+}$ , and  $\square$  represents a vacancy.

The  $Na_2O$  content in Grt I was mostly below the detection limit (Table 1), suggesting that  $REE^{3+}$  did not enter the garnet lattice via the first mechanism. Additionally, there was no clear correlation between the  $\Sigma REE$  content and  $Al_2O_3$  or  $MgO$  contents (Figure 10a,b), indicating that the second and third mechanisms were not the main mechanisms for  $REE^{3+}$  incorporation. Thus, it was inferred that the main mechanism for  $REE^{3+}$  incorporation into the Grt I lattice was the fourth mechanism. However, it was difficult to evaluate the fourth mechanism, and the  $REE^{3+}$  content in the Grt I lattice may have been influenced by both the crystal chemistry and the fluid's physical and chemical conditions, such as pH and  $fO_2$ . Similarly, the  $Na_2O$  content in Grt II was mostly below the detection limit (Table 1), indicating that the first mechanism was not the main mechanism for  $REE^{3+}$  incorporation into the Grt II lattice. The  $\Sigma REE$  content in Grt II showed a negative correlation with the  $Al_2O_3$  content and a positive correlation with the  $MgO$  content (Figure 10c,d), suggesting that  $REE^{3+}$  may substitute for  $Ca^{2+}$  and  $Al^{3+}$  to enter the Grt II lattice with  $Mg^{2+}$  via the third mechanism.

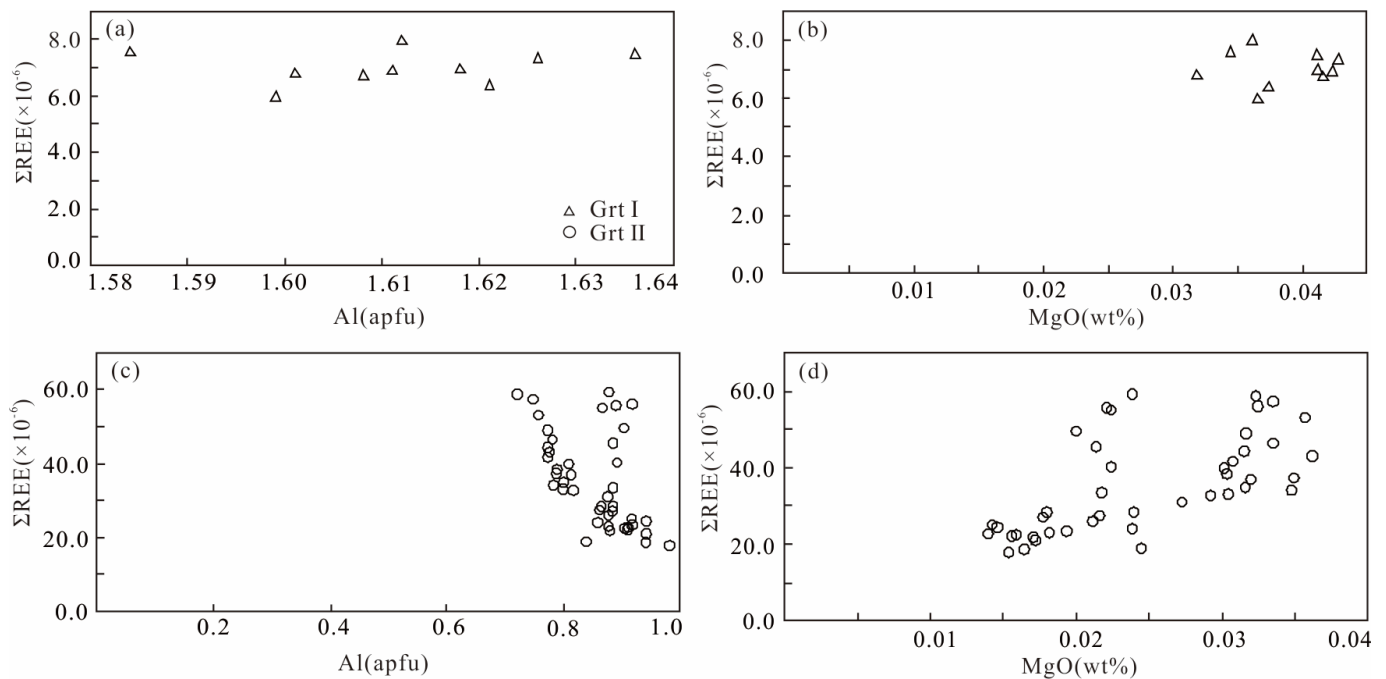


**Figure 10.** Plots of Al (a,c) and MgO (b,d) contents vs.  $\Sigma$ REE content in the garnets.

Y and  $\Sigma$ REEs have similar geochemical behaviors, and the linear correlation between the Y and  $\Sigma$ REE contents suggested that the garnets formed in a relatively closed system without fluid mixing. Conversely, deviations from the linear trend may have indicated changes in the fluid composition during garnet growth [5,40–45]. As shown in Figure 11, there was a linear correlation between the Y and  $\Sigma$ REE contents in both garnet generations, indicating that the compositions of the ore-forming fluids were stable. Some Grt II samples deviated slightly from the trend line, suggesting slight changes in the compositions of the ore-forming fluids in the late stage, but the ore-forming fluids were still dominated by magmatic-hydrothermal fluids.

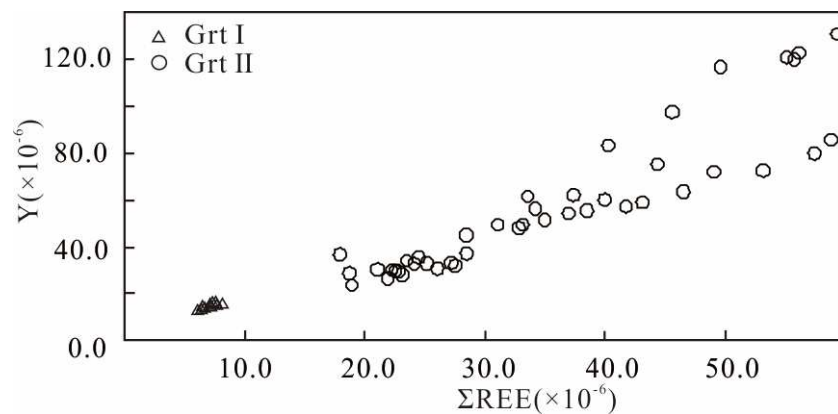


**Figure 11.** Diagram of  $\Sigma$ REE content vs. Y content in the garnets.

REE fractionation in garnet is closely related to the pH of the hydrothermal fluid [46]. When the fluid is mildly acidic, the REE pattern of garnet typically exhibits LREE enrichment, HREE depletion, and positive Eu anomalies [46–48]. In a neutral fluid, the REE pattern of garnet is HREE-enriched and LREE-depleted, with negative or no evident Eu anomalies [47]. As shown in Figure 9, both generations of garnet in the zinc–copper ore bodies of the Changpo–Tongkeng deposit displayed significant HREE enrichment, LREE depletion, and negative to no evident Eu anomalies, indicating that the two generations of garnet were formed under near-neutral conditions.

### 6.2. Characteristics of Ore Forming Based on Garnet Type

Garnets formed under different conditions have distinct chemical compositions, and these compositions can provide insight into the physicochemical conditions during their formation [3,49].

Due to the smaller ionic radius of  $\text{Fe}^{2+}$  compared to that of  $\text{Ca}^{2+}$ , it is difficult for  $\text{Fe}^{2+}$  to substitute for  $\text{Ca}^{2+}$  at the X-site in garnets through isomorphic substitution. As a result, under relatively reducing conditions, grossular is mainly formed, while most  $\text{Fe}^{2+}$  is transported in the hydrothermal fluids for long periods of time and over long distances in the form of  $\text{Na}(\text{FeCl})_4$  and other complexes [41,50]. In contrast, under relatively oxidizing conditions, the  $\text{Fe}^{2+}$  in hydrothermal fluids oxidizes to  $\text{Fe}^{3+}$ , substituting for  $\text{Al}^{3+}$  in garnet to form andradite, so the formation of andradite requires higher oxygen fugacity than grossular formation [30,51–53]. Additionally, under high oxygen fugacity, garnet can incorporate significant amounts of Sn, whereas Sn incorporation into garnet is difficult under low oxygen fugacity conditions [54].

Grt I was mainly composed of Al-rich garnet (avg.  $\text{Gr}_{072}\text{And}_{25}$ ), while Grt II was composed of Fe-rich garnet (avg.  $\text{Gr}_{039}\text{And}_{59}$ ). The average Sn content in Grt II (2377.65 ppm) was significantly higher than that in Grt I (439.02 ppm), and there was a gradual increase in the content of the andradite endmember from the core to the rim of Grt II (Figure 7d), reflecting that the oxygen fugacity of the ore-forming fluids gradually increased. Previous studies have shown that the host rocks of zinc–copper ore bodies contain abundant carbonaceous organic matter [8,9,55]. The ore-forming fluids exsolved from the magma interacted with the host rock and experienced a significant decrease in oxygen fugacity. As the carbonaceous organic matter in the host rock was gradually consumed, its impact on the ore-forming fluids gradually decreased, and the oxygen fugacity of the ore-forming fluids increased.

The absence of well-developed zoning in Grt I indicated a slow mineral crystallization rate and low water/rock ratio (W/R) during the crystal growth process, suggesting diffusion-controlled metasomatism and formation under relatively stable, closed conditions. Conversely, Grt II contained well-developed oscillatory zoning, indicating that it rapidly crystallized through infiltration-controlled metasomatism under high W/R conditions [4,56].

### 6.3. The Occurrence State of Ore-Forming Elements and Metallogenic Implications

The trace element analysis showed that the Sn content in the garnets was relatively high, with an average content of 439.02 ppm in Grt I and 2828.50 ppm in Grt II. The Sn content tended to be positively correlated with the content of the andradite component in garnet (Table 2). Previous studies have demonstrated that  $\text{Sn}^{4+}$  (0.069 nm) and  $\text{Fe}^{3+}$  (0.065 nm) have similar ionic radii, and Sn mainly enters garnet through isomorphic substitution of Fe, that is,  $\text{Sn}^{4+} + \text{Fe}^{2+} = 2\text{Fe}^{3+}$  [57–61]. When the oxygen fugacity falls within the MH (magnetite-hematite)–NNO (nickel-nickel oxide) range, Sn enters garnet as  $\text{Sn}^{4+}$  substituting for  $\text{Fe}^{3+}$ . However, when the oxygen fugacity is below the FMQ (fayalite-magnetite-quartz) range, it is difficult for Sn to enter garnet as  $\text{Sn}^{2+}$ ; therefore, Sn is enriched in the hydrothermal fluids [54].

In this paper, we collected the average Sn content in garnets from the Xianghualing, Baiganhu, Gejiu, and Huangshaping skarn-type tin deposits, which were 4294.79 ppm [62], 964.75 ppm [63], 2020.00 ppm [64], and 2109.24 ppm [30], respectively. The average Sn content in garnet from the zinc–copper ore bodies of the Changpo–Tongkeng deposit was 2377.65 ppm, which was comparable to that in the above mentioned tin deposits. Combined with high Sn content in vesuviante (Sn = 688.09 ppm, [65]) and axinite (Sn = 280.56 ppm, unpublished data) in this deposit, the results indicated that the ore-forming fluids were significantly enriched in Sn.

To date, In has been found in garnets from various types of skarn deposits, but there is limited research on In in garnet [39,63,66,67]. The average In content was 12.54 ppm in garnets from the zinc–copper ore bodies of the Changpo–Tongkeng deposit, with an

average content of 22.84 ppm in Grt II, which was 228 times higher than the Clark value [68]. There was a rough positive correlation between the Sn and In contents. Zhou J.H. et al. [63] and Fei X.H. et al. [39] reported average In contents of 7.77 and 7.86 ppm, respectively, in garnets from the Baiganhu and Cuihongshan deposits. The high In content in the garnets from the Changpo–Tongkeng deposit indicated that there was a large amount of In in the ore-forming fluids. In a study of the trace element In in the Dachang ore field, Wu Y.T. [69] noted that the In content in the ore-bearing strata was relatively high (avg. 1.88 ppm), with an average of 4.64 ppm in the Luofu Formation ( $D_2^2l$ ), especially in light-gray limestone where In was highly enriched (avg. 30.62 ppm). This enrichment was believed to have been influenced by the ore-forming fluids, and the study also revealed that the In content increased as the ore bodies approached the granitic pluton, indicating that In was mainly derived from magmatic-hydrothermal fluids.

The isotopic chronology showed that the metallogenic ages of the tin polymetallic ore bodies and zinc–copper ore bodies were consistent with the diagenetic age of the Longxianggai granitic pluton [8,10–15]. The  $\delta^{66}\text{Zn}$  value of sphalerite from the zinc–copper ore bodies measured by Cai M.H. [17] was 0.24‰–0.34‰, while that of the tin polymetallic ore bodies was 0.22‰–0.31‰. The zinc isotopic compositions of the two types of ore bodies were quite consistent and were consistent with granitic pluton. In addition, the REE patterns of sphalerites in the two types of ore bodies were consistent with granitic pluton, which is characterized by LREE enrichment and HREE depletion [70]. Wu Y.T. [69] analyzed the Sn content in the No. 96 and No. 95 zinc–copper ore bodies and No. 92 and No. 91 tin polymetallic ore bodies and found that the average Sn content in different ore bodies did not change significantly, with values of 114.18, 119.02, 134.58, and 113.4 ppm, respectively. The above results indicated that the ore-forming material sources of zinc–copper ore bodies and tin polymetallic ore bodies were the same and derived from the Longxianggai granitic pluton. The high Sn content in garnet may be the main reason for the lack of tin ore bodies in the skarn stage.

As previously mentioned, the strike of the concealed granitic pluton of the Changpo–Tongkeng deposit is consistent with the strike of the Dachang fault. Both the granitic pluton and the ore bodies occur on the gentle NE limb of the Dachang anticline. The zinc–copper ore bodies occur in the contact zone between the granitic pluton and the marl and limestone of the Luofu Formation ( $D_2^2l$ ). Tin polymetallic ore bodies are found in the siliceous rocks of the Upper Devonian Liujian Formation ( $D_3^1l$ ), the limestone of the Wuzhishan Formation ( $D_3^2w$ ), and the marl of the Tongchejiang Formation ( $D_3^3t$ ), which are far from the granitic pluton. The zinc–copper ore bodies are located proximal to the granitic pluton in the lower part, with a relatively closed, high-pressure and high-temperature ore-forming system [21]. Moreover, the ore-forming strata contain abundant carbonaceous organic matter and sulfur [8,9,55], which leads to a decrease in the fluid's oxygen fugacity and an increase in its sulfur fugacity. These conditions are unfavorable for the precipitation of cassiterite but cause sulfides to precipitate and form zinc–copper deposits. With the continuous exsolution of magmatic-hydrothermal fluids, the ore-forming fluids migrated upwards along the Dachang fault and fractured zones. As the fluid pressure decreased, fluid boiling became likely, and the fluids could mix with atmospheric precipitation infiltrating along the fault and fractured zones. Fluid water rock reactions were enhanced, leading to tin precipitation [71–76]. Analysis of the fluid inclusions and the C, H, O, and Ar isotopes of the minerals also suggested the addition of atmospheric precipitation and the boiling of ore-forming fluids during tin precipitation [8,21].

In this study, we collected the trace element contents of garnets from skarn tin (–tungsten) deposits and copper (–polymetallic) deposits in China (Figure 12). The Sn content in garnet from the tin (–tungsten) deposits was 100–10,000 ppm, with  $\delta\text{Eu}$  less than 1; the Sn content from the copper (–polymetallic) deposits was generally less than 1000 ppm (a high Sn content occurs in the Huangshaping and Haobugao deposits because the deposits are accompanied by cassiterite), and  $\delta\text{Eu}$  was typically greater than 1. As seen from the above discussion, the trace element contents of garnet in skarn-type deposits,

such as Sn, along with  $\delta\text{Eu}$  and other indicators played a significant role in evaluating the mineralization type and mineralization potential.

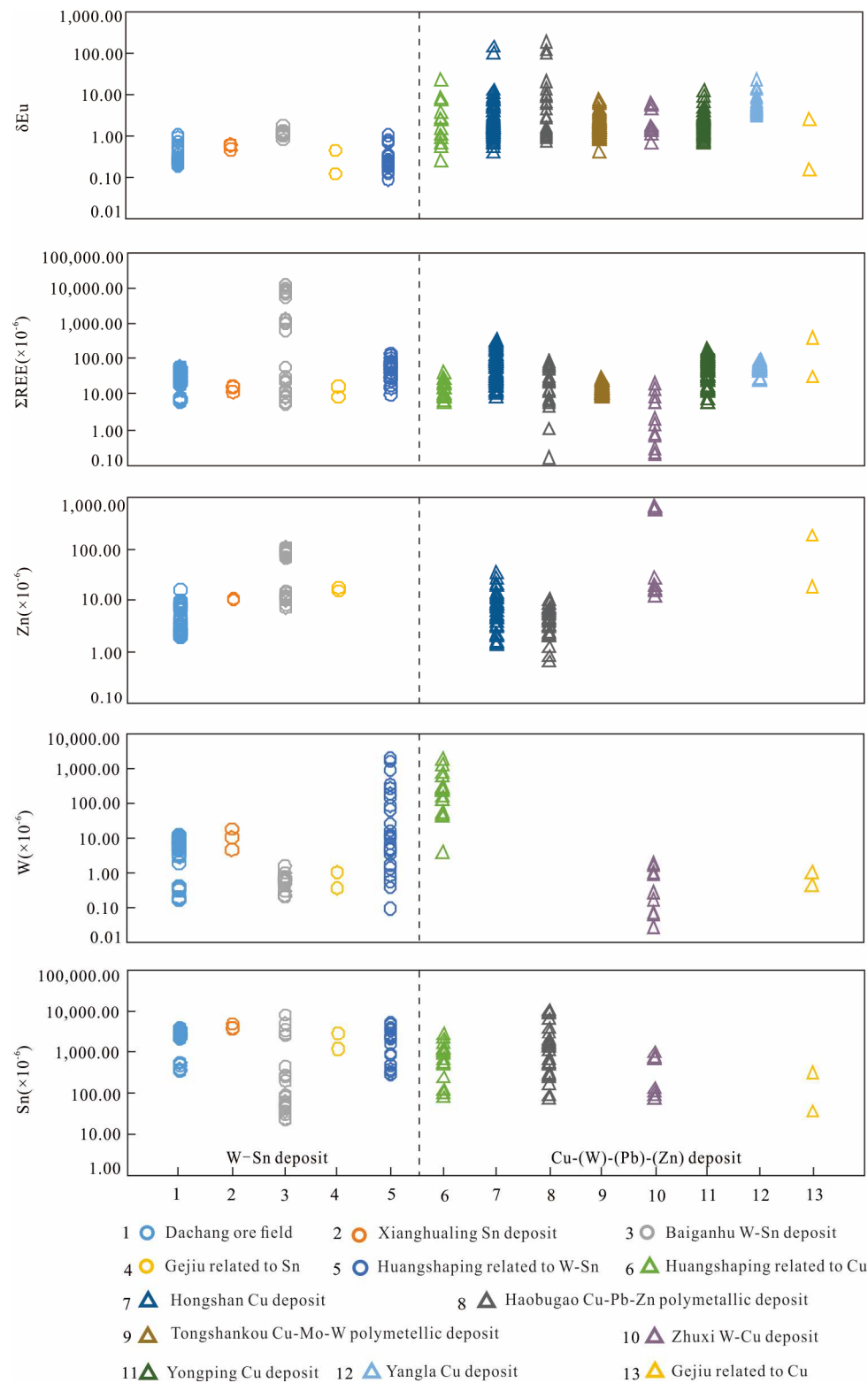


**Figure 12.** Variation range diagrams of ore-forming element contents,  $\Sigma\text{REE}$  content, and  $\delta\text{Eu}$  in garnets from different types of skarn deposits. Data source: This study and [2,30,35,62–64,77–80].

## 7. Conclusions

- (1) Garnets in the zinc–copper ore bodies in the Changpo–Tongkeng deposit belong to the grossular–andradite solid solution series, which can be divided into two generations: an early generation (Grt I) and a late generation (Grt II). Grt I has uniform composition and no zoning. It was mainly formed in a relatively closed, near-neutral metallogenic system with low oxygen fugacity that was dominated by hydrothermal diffusion metasomatism. Grt II is andradite with well-developed oscillatory zoning, which was formed in a near-neutral system with relatively high oxygen fugacity that was dominated by infiltration metasomatism.
- (2) Both garnet generations are strongly depleted in LILEs and enriched in HFSEs such as Hf, Zr, Nb, and Ta; the total contents of REEs in the two generations of garnet are relatively low, showing LREE depletion and HREE enrichment patterns, and Grt II has higher REE contents than Grt I. REE<sup>3+</sup> enters Grt I through isomorphism by replacing Ca<sup>2+</sup> and may be influenced by both the crystal chemistry and the fluid's physical and chemical conditions (pH, *f*O<sub>2</sub>). REE<sup>3+</sup> may substitute for Ca<sup>2+</sup> and Al<sup>3+</sup> and enter the Grt II lattice with Mg<sup>2+</sup>.
- (3) The contents of Sn, As, W, In, and Ge in the garnets are relatively high and increase with an increase in the andradite component. Sn in zinc–copper ore bodies mainly exists in the form of isomorphic substitution in garnet, which may be the main reason for the lack of tin ore bodies during the skarn stage.
- (4) Based on the trace element analysis of garnets from domestic skarn tin (–tungsten) deposits and copper (–polymetallic) deposits, the Sn content and δEu in garnet can be used to evaluate the tin-forming potential of skarn deposits.

**Author Contributions:** The article was originally written and the experiments were designed by L.H. and the manuscript was revised by T.L., D.W. and Z.Z., B.L. conducted the fieldwork. J.G. and J.C. digitalized the geological map along with L.H. All authors have read and agreed to the published version of the manuscript.

**Funding:** This study was financially supported by the China Geological Survey granted to T. Liang (Grant Number: DD20221695-43, DD20190379).

**Data Availability Statement:** The raw/processed data required to reproduce these findings cannot be shared at this time as the data also forms part of an ongoing study.

**Acknowledgments:** We would like to express our sincere gratitude to Xijuan Tan from Chang'an University for sample analysis processes. We also thank the three anonymous reviewers and an academic editor for their constructive comments on the manuscript.

**Conflicts of Interest:** The authors declare no conflict of interest.

## References

1. Yu, F.; Shu, Q.H.; Zeng, Q.W.; Ma, X.H.; Niu, X.D.; Ma, S.L.; Li, Y.X.; Xing, K. Chemical composition of garnet from the Xintianling skarn W deposit in southern Hunan and its geological significance. *Acta Petrol. Sin.* **2022**, *38*, 78–90. (In Chinese with English abstract)
2. Bian, X.L.; Zhang, J.; Wang, J.L.; Liu, C.F.; Yu, H.J. In Situ analysis of garnets from the Hongshan skarn copper deposit in Northwest Yunnan Province and its geological implications. *Acta Petrol. Sin.* **2019**, *35*, 1463–1477. (In Chinese with English abstract)
3. Jamtveit, B.; Wogelius, R.A.; Fraser, D.G. Zonation patterns of skarn garnets: Records of hydrothermal system evolution. *Geology* **1993**, *21*, 113–116. [[CrossRef](#)]
4. Smith, M.P.; Henderson, P.; Jeffries, T.E.R.; Long, J.; Williams, C.T. The rare earth elements and uranium in garnets from the Beinn an Dubhaich Aureole, Skye, Scotland, UK: Constraints on processes in a dynamic hydrothermal system. *J. Petrol.* **2004**, *45*, 457–484. [[CrossRef](#)]
5. Gaspar, M.; Knaack, C.; Meinert, L.D.; Moretti, R. REE in skarn systems: A LA-ICP-MS study of garnets from the Crown Jewel gold deposit. *Geochim. Cosmochim. Acta* **2008**, *72*, 185–205. [[CrossRef](#)]
6. Shu, Q.H.; Lai, Y.; Sun, Y.; Wang, C.; Meng, S. Ore genesis and hydrothermal evolution of the Baiyinnuo'er zinc-lead skarn deposit, Northeast China: Evidence from isotopes (S, Pb) and fluid inclusions. *Econ. Geol.* **2013**, *108*, 835–860. [[CrossRef](#)]

7. Karimzadeh Somarin, A. Garnet composition as an indicator of Cu mineralization: Evidence from skarn deposits of NW Iran. *J. Geochem. Explor.* **2004**, *81*, 47–57. [[CrossRef](#)]
8. Liang, T. Study on the Metallogenic Mechanism of Changpo-Tongkeng Tin-polymetallic Deposit, Dachang, Guangxi. Ph.D. Thesis, Chang'an University, Xi'an, China, 2008. (In Chinese with English abstract)
9. Chen, Y.C.; Huang, M.Z.; Xu, J.; Hu, Y.Z.; Tang, S.H.; Li, Y.Q.; Meng, L.K. *Geology of Dachang Tin Deposit*; Geological Publishing House: Beijing, China, 1993; pp. 1–361. (In Chinese)
10. Guo, J.; Zhang, R.Q.; Sun, W.D.; Ling, M.X.; Hu, Y.B.; Wu, K.; Luo, M.; Zhang, L.C. Genesis of tin-dominant polymetallic deposits in the Dachang district, South China: Insights from cassiterite U-Pb ages and trace element compositions. *Ore Geol. Rev.* **2018**, *95*, 863–879. [[CrossRef](#)]
11. Wang, D.H.; Chen, Y.C.; Chen, W.; Sang, H.Q.; Li, H.Q.; Lu, Y.F.; Chen, K.L.; Lin, Z.M. Dating the Dachang Giant Tin-Polymetallic Deposit in Nandan, Guangxi. *Acta Geol. Sin.* **2004**, *78*, 132–138. (In Chinese with English abstract)
12. Liang, T.; Wang, D.H.; Li, H.Q.; Huang, M.H.; Wang, D.M.; Yu, P.; Cai, M.H. REE geochemistry and Sm-Nd isotope age of garnet from the Dachang, Guangxi. *J. Northwest Univ.* **2011**, *41*, 676–681. (In Chinese with English abstract)
13. Huang, W.T.; Liang, H.Y.; Zhang, J.; Wu, J.; Chen, X.L.; Ren, L. Genesis of the Dachang Sn-polymetallic and Baoshan Cu ore deposits, and formation of a Cretaceous Sn-Cu ore belt from southwest China to western Myanmar. *Ore Geol. Rev.* **2019**, *112*, 103030. [[CrossRef](#)]
14. Wang, T.Y.; Li, G.J.; Wang, Q.F.; Santosh, M.; Zhang, Q.Z.; Deng, J. Petrogenesis and metallogenic implications of Late Cretaceous I- and S-type granites in Dachang-Kunlun ore belt, southwestern South China Block. *Ore Geol. Rev.* **2019**, *113*, 103079. [[CrossRef](#)]
15. Guo, J.; Wu, K.; Seltmann, R.; Zhang, R.Q.; Ling, M.X.; Li, C.Y.; Zhang, L.P.; Sun, W.D. Unraveling the link between mantle upwelling and formation of Sn-bearing granitic rocks in the world-class Dachang tin district, South China, Geological Society of America. *Bulletin* **2022**, *134*, 1043–1064. [[CrossRef](#)]
16. Cai, M.H.; Mao, J.W.; Ting, L.; Franco, P.; Huang, H.L. The origin of the Tongkeng-Changpo tin deposit, Dachang metal district, Guangxi, China: Clues from fluid inclusions and He isotope systematics. *Miner. Depos.* **2007**, *42*, 613–626. [[CrossRef](#)]
17. Cai, M.H.; Peng, Z.A.; Hu, Z.S.; Li, Y. Zn, He-Ar and Sr-Nd isotopic compositions of the Tongkeng Tin-polymetallic ore deposit in south China: Implication for ore genesis. *Ore Geol. Rev.* **2020**, *124*, 103605. [[CrossRef](#)]
18. Guo, J.; Zhang, G.Y.; Xiang, L.; Zhang, R.Q.; Zhang, L.P.; Sun, W.D. Combined mica and apatite chemical compositions to trace magmatic-hydrothermal evolution of fertile granites in the Dachang Sn-polymetallic district, South China. *Ore Geol. Rev.* **2022**, *151*, 105168. [[CrossRef](#)]
19. Zhang, J.; Huang, W.T.; Chen, X.L.; Wu, J.; Ren, L.; Liang, H.Y.; Chen, L. Different Geochemical Characteristics and Genetic Link between Sn-polymetallic Deposit and Skarn Zn-Cu Deposit in the Dachang Ore Field, Guangxi. *Geotecton. Metallog.* **2019**, *43*, 1186–1199. (In Chinese with English abstract)
20. Zhao, K.D.; Zhang, L.H.; Palmer, M.R.; Jiang, S.Y.; Xu, C.; Zhao, H.D.; Chen, W. Chemical and boron isotopic compositions of tourmaline at the Dachang Sn-polymetallic ore district in South China: Constraints on the origin and evolution of hydrothermal fluids. *Miner. Depos.* **2021**, *56*, 1589–1608. [[CrossRef](#)]
21. Li, Y.Q.; Chen, W.S. The Ore-forming Fluid of Dachang Tin Deposit. *Acta Petrol. Sin.* **1989**, *5*, 12–24. (In Chinese with English abstract)
22. Li, M.Q.; Shui, Z.F. Geochemical characteristics of stable isotope in Lamo zinc copper polymetallic deposit, Guangxi. *Geol. Geochem.* **1994**, *4*, 66–70. (In Chinese with English abstract)
23. Li, M.Q. A Geochemical Study on The Fluid Inclusion of The Lamo Zn-Cu Polymetallic Deposit in Guangxi, China. *J. Guizhou Inst. Technol.* **1995**, *24*, 55–59. (In Chinese with English abstract)
24. Fu, M.; Changkakoti, A.; Krouse, H.R.; Gray, J.; Kwak, T.A.P. An oxy-gen, hydrogen, sulfur, and carbon isotope study of carbonate-replacement (skarn) tin deposits of the Dachang tin field, China. *Econ. Geol.* **1991**, *86*, 1683–1703. [[CrossRef](#)]
25. Fu, M.; Kwak, T.A.P.; Mernagh, T.P. Fluid inclusion studies of zoning in the Dachang tin-polymetallic ore field. *People's Republic China. Econ. Geol.* **1993**, *88*, 283–300.
26. Sun, S.S.; McDonough, W.F. Chemical and isotopic systematics of oceanic basalts: Implications for mantle composition and processes. *Geol. Soc. Lond. Spec. Publ.* **1989**, *42*, 313–345. [[CrossRef](#)]
27. Menzer, G. XX. Die kristallstruktur der granate. *Zeitschrift Fur Krist.* **1926**, *63*, 157–158. [[CrossRef](#)]
28. Meinert, L.D.; Hefton, K.K.; Mayes, D.; Tasiran, I. Geology, zonation, and fluid evolution of the Big Gossan Cu-Au skarn deposit, Ertzberg district, Irian Jaya. *Econ. Geol.* **1997**, *92*, 509–534. [[CrossRef](#)]
29. McIntire, W.L. Trace element partition coefficients: A review of theory and applications to geology. *Geochim. Cosmochim. Acta* **1963**, *27*, 1209–1264. [[CrossRef](#)]
30. Zhao, P.L.; Yuan, S.D.; Yuan, S.D. Geochemical characteristics of garnet in the Huangshaping polymetallic deposit, southern Hunan: Implications for the genesis of Cu and W-Sn mineralization. *Acta Petrol. Sin.* **2018**, *34*, 2581–2597. (In Chinese with English abstract)
31. Wen, G.; Li, J.W.; Hofstra, A.H.; Koenig, A.E.; Cui, B.Z. Textures and compositions of clinopyroxene in an Fe skarn with implications for ore-fluid evolution and mineral-fluid REE partitioning. *Geochim. Cosmochim. Acta* **2020**, *290*, 104–123. [[CrossRef](#)]
32. Huang, X.D.; Lu, J.J.; Zhang, R.Q.; Sizaret, S.; Ma, D.S.; Wang, R.C.; Zhu, X.; He, Z.Y. Garnet and scheelite chemistry of the Weijia tungsten deposit, South China: Implications for fluid evolution and W skarn mineralization in F-rich ore system. *Ore Geol. Rev.* **2022**, *142*, 104729. [[CrossRef](#)]

33. Enami, M.; Cong, B.; Yoshida, T.; Kawabe, I. A mechanism for Na incorporation in garnet: An example from garnet in orthogneiss from the Su-Lu Terrane, eastern China. *Am. Mineral.* **1995**, *80*, 475–482. [[CrossRef](#)]
34. Sepidbar, F.; Mirnejad, H.; Li, J.W.; Wei, C.J.; George, L.L.; Burlinson, K. Mineral geochemistry of the Sangan skarn deposit, NE Iran: Implication for the evolution of hydrothermal fluid. *Geochemistry* **2017**, *77*, 399–419. [[CrossRef](#)]
35. Tian, Z.D.; Leng, C.B.; Zhang, X.C.; Zafar, T.; Zhang, L.J.; Hong, W.; Lai, C.K. Chemical composition, genesis and exploration implication of garnet from the Hongshan Cu-Mo skarn deposit, SW China. *Ore Geol. Rev.* **2019**, *112*, 103016. [[CrossRef](#)]
36. Hong, J.X.; Zhang, H.Y.; Li, D.F.; Ouyang, Y.P.; Zhai, D.G.; Liu, F.; Liu, J.J. In Situ LA-ICP-MS U-Pb geochronology and geochemical characteristics of garnet from the Zhuxi skarn W-Cu deposit, South China. *Ore Geol. Rev.* **2022**, *140*, 104577. [[CrossRef](#)]
37. Xie, S.X.; Yang, L.Q.; He, W.Y.; Gao, X. Garnet trace element geochemistry of Yangla Cu deposit in NW Yunnan, China: Implications for multistage ore-fluid activities in skarn system. *Ore Geol. Rev.* **2022**, *141*, 104662. [[CrossRef](#)]
38. Ismail, R.; Ciobanu, C.L.; Cook, N.J.; Teale, G.S.; Giles, D.; Mumm, A.S.; Wade, B. Rare earths and other trace elements in minerals from skarn assemblages, Hillside iron oxide-copper-gold deposit, Yorke Peninsula, South Australia. *Lithos* **2014**, *184–187*, 456–477. [[CrossRef](#)]
39. Fei, X.H.; Zhang, Z.C.; Cheng, Z.G.; Santosh, M. Factors controlling the crystal morphology and chemistry of garnet in skarn deposits: A case study from the Cuihongshan polymetallic deposit, Lesser Xing'an Range, NE China. *Am. Mineral.* **2019**, *104*, 1455–1468. [[CrossRef](#)]
40. Wood, S.A. The geochemistry of rare earth elements and yttrium in geothermal waters. *Spec. Publ. Soc. Econ. Geol.* **2003**, *10*, 133–158.
41. Wang, W.; Wang, M.F.; Liu, K.; Guo, X.N. The current status and prospects of the study of garnet in skarn for hydrothermal fluid evolution tracing and mineralization zoning. *Acta Petrol. Mineral.* **2016**, *35*, 147–161. (In Chinese with English abstract)
42. Dziggel, A.; Wulff, K.; Kolb, J.; Meyer, F.M.; Lahaye, Y. Significance of oscillatory and bell-shaped growth zoning in hydrothermal garnet: Evidence from the Navachab gold deposit, Namibia. *Chem. Geol.* **2009**, *262*, 262–276. [[CrossRef](#)]
43. Zhai, D.G.; Liu, J.J.; Zhang, H.Y.; Wang, J.P.; Su, L.; Yang, X.A.; Wu, S.H. Origin of oscillatory zoned garnets from the Xieertala Fe-Zn skarn deposit, northern China: In situ LA-ICP-MS evidence. *Lithos* **2014**, *190*, 279–291. [[CrossRef](#)]
44. Park, C.; Song, Y.; Kang, I.M.; Shim, J.; Chung, D.; Park, C.S. Metasomatic changes during periodic fluid flux recorded in grandite garnet from the Weondong W-skarn deposit, South Korea. *Chem. Geol.* **2017**, *451*, 135–153. [[CrossRef](#)]
45. Xiao, X.; Zhou, T.F.; White, N.C.; Zhang, L.J.; Fan, Y.; Wang, F.Y.; Chen, X.F. The formation and trace elements of garnet in the skarn zone from the Xinqiao Cu-S-Fe-Au deposit, Tongling ore district, Anhui Province, eastern China. *Lithos* **2018**, *302–303*, 467–479. [[CrossRef](#)]
46. Bau, M. Rare-earth element mobility during hydrothermal and metamorphic fluid rock interaction and the significance of the oxidation-state of europium. *Chem. Geol.* **1991**, *93*, 219–230. [[CrossRef](#)]
47. Zhang, Y.; Shao, Y.J.; Wu, C.D.; Chen, H.Y. LA-ICP-MS trace element geochemistry of garnets: Constraints on hydrothermal fluid evolution and genesis of the Xinqiao Cu-S-Fe-Au deposit, eastern China. *Ore Geol. Rev.* **2017**, *86*, 426–439. [[CrossRef](#)]
48. Gao, X.Q.; Sun, X.M.; Fu, Y.; Liu, Q.F. Garnet geochemistry of the giant Beiya gold-polymetallic deposit in SW China: Insights into fluid evolution during skarn formation. *Ore Geol. Rev.* **2022**, *150*, 105198. [[CrossRef](#)]
49. Meinert, L.D. Skarns and skarn deposits. *Geosci. Can.* **1992**, *19*, 145–162.
50. Li, Y.H.; Xie, G.Q.; Duan, C.; Han, D.; Wang, C.Y. Effect of sulfate evaporatesalt layer over the formation of skarn type iron ores. *Acta Geol. Sin.* **2013**, *7*, 1324–1334. (In Chinese with English abstract)
51. Peng, H.J.; Li, H.Y.; Pei, R.F.; Zhang, C.Q.; Zhou, Y.M.; Tian, G.; Li, J.X.; Long, F. Mineralogical characteristics and metallogeny of the Hongni-Hongshan copper deposit in Zhongdian area, Yunnan Province, China. *Acta Petrol. Sin.* **2014**, *30*, 237–256, (In Chinese with English abstract).
52. Zhu, Q.Q.; Xie, G.Q.; Li, W.; Zhang, F.; Wang, J.; Zhang, P.; Yu, B.F. In Situ analysis of garnets from the Jinshandian iron skarn deposit, Hubei Province, and its geological implications. *Geol. China* **2014**, *41*, 1944–1963. (In Chinese with English abstract)
53. Xie, G.Q.; Mao, J.W.; Zhu, Q.Q.; Yao, L.; Li, Y.H.; Li, W.; Zhao, H.J. Geochemical constraints on Cu-Fe and Fe skarn deposits in the E'dong district, Middle-Lower Yangtze River metallogenic belt, China. *Ore Geol. Rev.* **2015**, *64*, 425–444. [[CrossRef](#)]
54. Eadington, P.J.; Kinealy, K. Some aspects of the hydrothermal reactions of tin during skarn formation. *J. Geol. Soc. Aust.* **1983**, *30*, 461–471. [[CrossRef](#)]
55. Jan, P.; Bohdan, K.; Petr, D.; Ivan, V.; Karel, Z.; Fan, D.L.; Zhang, T.; Marie-christine, B. Tin-polymetallic sulfide deposits in the eastern part of the Dachang tin field (South China) and the role of black shales in their origin. *Miner. Depos.* **2003**, *38*, 39–66.
56. Jamtveit, B.; Hervig, R.L. Constraints on transport and kinetics in hydrothermal systems from zoned garnet crystals. *Science* **1994**, *263*, 505–507. [[CrossRef](#)] [[PubMed](#)]
57. McIver, J.R.; Mihalik, P. Stannian andradite from “Davib Ost”, South West Africa. *Can. Miner.* **1975**, *13*, 217–221.
58. Butler, B.C.M. Tin-rich garnet, pyroxene, and spinel from a slag. *Mineral. Mag.* **1978**, *42*, 487–492. [[CrossRef](#)]
59. Amthauer, G.; McIver, J.R.; Viljoen, E.A. <sup>57</sup>Fe and <sup>119</sup>Sn Mössbauer studies of natural tin-bearing garnets. *Phys. Chem. Miner.* **1979**, *4*, 235–244. [[CrossRef](#)]
60. Plimer, L.R. Malayaite and tin-bearing silicates from a skarn at Doradilla via Bourke, New South Wales. *Aust. J. Earth Sci.* **1984**, *31*, 147–153. [[CrossRef](#)]
61. Chen, J.; Wu, H. Synthetic analogue experiments on the Shizhuyuan tungsten, tin, molybdenum and bismuth skarn deposit in southeastern Hunan province. *Miner. Depos.* **1988**, *7*, 32–41. (In Chinese with English abstract)

62. Yu, F.; Shu, Q.H.; Niu, X.D.; Xing, K.; Li, L.L.; Lentz, D.R.; Zeng, Q.W.; Yang, W.J. Composition of Garnet from the Xianghualing Skarn Sn Deposit, South China: Its Petrogenetic Significance and Exploration Potential. *Minerals* **2020**, *10*, 456. [[CrossRef](#)]
63. Zhou, J.H.; Feng, C.Y.; Li, D.X. Geochemistry of the garnets in the Baiganhu W-Sn orefield, NW China. *Ore Geol. Rev.* **2017**, *82*, 70–92. [[CrossRef](#)]
64. Zhang, Y.P.; Shao, Y.J.; Xiong, Y.Q.; Xi, Z.J.; Lu, L.; Zhang, M.; Mao, Y.J. Metallogenic indication from geochemical characteristics of garnet in Gejiu Sn-Cu ore-concentrated area, Yunnan Province. *Miner. Depos.* **2022**, *41*, 682–701, (In Chinese with English abstract).
65. Yang, W.Q.; Zheng, X.J.; Yang, G.S.; Yan, Y.F.; Sun, B. The geological significance of vesuvianite in the Heishuigou Zn-Cu deposit in the Dachang area, Guangxi Autonomous Region, China. *Acta Mineral. Sin.* **2022**, *42*, 193–202, (In Chinese with English abstract).
66. Xu, J.; Ciobanu, C.L.; Cook, N.J.; Zheng, Y.Y.; Sun, X.; Wade, B.P. Skarn formation and trace elements in garnet and associated minerals from Zhibula copper deposit, Gangdese Belt, southern Tibet. *Lithos* **2016**, *262*, 213–231. [[CrossRef](#)]
67. Li, X.F.; Zhu, Y.T.; Xu, J. Indium as a critical mineral: A research progress report. *Chin. Sci. Bull.* **2020**, *65*, 3678–3687, (In Chinese with English abstract). [[CrossRef](#)]
68. Taylor, S.R.; McLennan, S.M. The continental crust: Its composition and evolution. *J. Geol.* **1985**, *94*, 57–72.
69. Wu, Y.T. Study on the Enrichment Regularity of Indium in Dachang Ore-Field, Guangxi. Ph.D. Thesis, Central South University, Changsha, China, 2009. (In Chinese with English abstract).
70. Zhang, H. Geochemical Characteristics of Sphalerite and Zn Isotope Study in Tongkeng Tin Polymetallic Deposit, Dachang, Guangxi. Master's Thesis, Guangxi University, Guangxi, China, 2019. (In Chinese with English abstract).
71. Wilson, G.A.; Eugster, H.P. Cassiterite solubility and tin speciation in supercritical chloride solutions. *Geochem. Soc. Spec. Publ.* **1990**, *2*, 179–195.
72. Wang, L.J.; Wang, J.B.; Wang, Y.W.; Long, L.L. Metallogenic mechanism of fluid and prospecting forecast of Dajing Sn-Cu polymetallic deposit, Inner Mongolia. *Acta Petrol. Sin.* **2015**, *31*, 991–1001, (in Chinese with English abstract).
73. Zhang, R.Q.; Lu, J.J.; Lehmann, B.; Li, C.Y.; Li, G.L.; Zhang, L.P.; Guo, J.; Sun, W.D. Combined zircon and cassiterite U-Pb dating of the Piaotang granite-related tungsten-tin deposit, southern Jiangxi tungsten district, China. *Ore Geol. Rev.* **2017**, *82*, 268–284. [[CrossRef](#)]
74. Schmidt, C. Formation of hydrothermal tin deposits: Raman spectroscopic evidence for an important role of aqueous Sn (IV) species. *Geochim. Cosmochim. Acta* **2018**, *220*, 499–511. [[CrossRef](#)]
75. Yuan, S.D.; Zhao, P.L.; Liu, M. Some problems involving in petrogenesis and metallogenesis of granite-related tin deposits. *Miner. Depos.* **2020**, *39*, 607–618, (In Chinese with English abstract).
76. Liu, X.C.; Yu, P.P.; Xiao, C.H. Tin transport and cassiterite precipitation from hydrothermal fluids. *Geosci. Front.* **2023**, *14*, 101624. [[CrossRef](#)]
77. Chu, G.B.; Chen, H.Y.; Zhang, S.T.; Zhang, Y.; Chen, J.M. Geochemistry and geochronology of multi-generation garnet: New insights on the genesis and fluid evolution of prograde skarn formation. *Geosci. Front.* **2023**, *14*, 101495. [[CrossRef](#)]
78. Ouyang, Y.P.; Zhou, X.R.; Yao, Z.Y.; Rao, J.F.; Song, S.W.; Wei, J.; Lu, Y. Study on the two stage garnets and their indication of mineralization in the Zhuxi W(Cu) deposit, northeastern Jiangxi Province. *Earth Sci. Front.* **2020**, *27*, 219–231, (In Chinese with English abstract).
79. Fan, X.J.; Wang, X.D.; Lv, X.B.; Wei, W.; Chen, W. Garnet composition as an indicator of skarn formation: LA-ICP-MS and EPMA studies on oscillatory zoned garnets from the Haobugao skarn deposit, Inner Mongolia, China. *Geol. J.* **2019**, *54*, 1976–1992. [[CrossRef](#)]
80. Tian, M.J.; Li, X.C.; Guo, J.H.; Li, Y.G.; Zhang, Y. Composition of garnet from the Yongping Cu skarn deposit, South China: Implication for ore-fluid evolution. *Ore Geol. Rev.* **2021**, *139*, 104585. [[CrossRef](#)]

**Disclaimer/Publisher's Note:** The statements, opinions and data contained in all publications are solely those of the individual author(s) and contributor(s) and not of MDPI and/or the editor(s). MDPI and/or the editor(s) disclaim responsibility for any injury to people or property resulting from any ideas, methods, instructions or products referred to in the content.